On the influence of boundary conditions when determining transport coefficients from digital images of heterogeneous media.

Jean-François Thovert, Valeri V. Mourzenko

On the influence of boundary conditions when determining transport coefficients from digital images of heterogeneous media.

Jean-François Thovert[a,*], Valeri V. Mourzenko[a]

[a]*Institut P', CNRS - Université de Poitiers - ISAE-ENSMA, 11 bd Marie et Pierre Curie, TSA 41123, 86073 POITIERS CEDEX 9, France*

Abstract

Sensitivity to the boundary conditions (BC's) when determining macroscopic transport coefficients by numerical upscaling in finite domains is a well known methodological issue, explored here with the purpose of: quantifying the influence of the BC's in relation with the parameters of the system (porosity, characteristic length scale, conductivity contrast); assessing the level of confidence associated with the predictions; devising criteria to anticipate the risk of serious artifacts, and proposing ways to limit them. The terminology of thermal transfer is used but the developments apply to any transport mechanism governed by a diffusion equation, including conduction, mass diffusion or Darcy flow. Quantitative indicators are defined for a rigorous individual or comparative assessment of conductivity tensors, and used in the analysis of extensive numerical data obtained in tomographic images and model materials, with a broad range of properties. Practical criteria are proposed for the *a priori* and *a posteriori* detection of at-risk situations, and a self-diagnosing protocol is proposed to screen out the BC's influence, whenever possible.

Keywords: Numerical upscaling, Conductivity, Permeability, Boundary condition, Tomography, Undersampling

1. Introduction

Sensitivity to boundary conditions (BC's) is a well known issue when determining macroscopic transport coefficients by numerical upscaling, *i.e.*, by solving governing equations in a finite domain where the required fields of the local properties are provided, either for instance by X-ray tomographic imaging for core-scale samples [1], or from geophysical characterization techniques on the field-scale [2]. In the first case, with a full knowledge of the microscopic geometry, the upscaling of Stokes flow equations for the determination of a permeability tensor can be addressed (Stokes $\rightarrow$ Darcy), as well as any conduction or diffusion transport processus. In the latter case, the data are provided on a coarser scale where the flow properties are already described by a mesoscale permeability coefficient, and the secondary upscaling aims to determine a permeability tensor of the same nature but on a larger scale. We focus in this work on steady-state conduction-like processes, governed by Fourier, Ohm, Fick or Darcy laws, which are mathematically equivalent. A heat transfer terminology is used, but the word "conductivity" can be understood throughout this paper as thermal, electric, hydraulic or mass diffusivity, with temperature T replaced by potential, pressure or concentration (see Section 2.3).

The same question was addressed in the recent contribution [1], where four tomographic images of materials of various natures were used for a thorough assessment of the BC's influence. The present paper proceeds along the same lines and also considers synthetic media, which makes a systematic investigation of geometrical parameters possible and allows to formulate the phenomenological observations of [1] in a more general and quantitative way. In order to be reasonably self-contained, many definitions of mathematical and conceptual tools are repeated here but some elements are skipped for concision. Complementary bibliographical elements, phenomenological discussion and additional technical details can be found in [1].

Various procedures based on different kinds of boundary conditions have been used since the earliest days of numerical upscaling of heterogeneous system properties on the field scale [3] or on the core-scale based on tomographic

*Corresponding author

Email address: jean.francois.thovert@univ-poitiers.fr (Jean-François Thovert)

digital images [4], and the differences in the results of different approaches was often pointed out. The brief following review focuses on contributions which present systematic comparisons and/or address theoretical aspects of the issue.

The general review [5] of theoretical aspects of the upscaling techniques for Darcy flow in heterogeneneous media surveys various protocols and stresses the sensitivity of the resulting block permeability to the BC's. Darcy flow upscaling procedures are also extensively reviewed in [6], including the aspects associated with BC's and post-treatments. Periodicity, permeameter and immersion conditions (see Section 2.5), as well as others involving the introduction of border regions (see below and Section 2.8) are surveyed, and their relative merits and shortcomings are discussed. More recently, various BC's have been tested in [7] for the evaluation of the electrical conductivity of rock samples from tomographic images. It was stressed again that the choice of BC's is important, but no conclusion or advice was put forward.

The *undersampling* and *oversampling* approaches proceed from the same idea in the search of an intrinsic value of an effective conductivity. In the former, the sampling domain is reduced by excluding from the measurements a peripheral layer so that boundary effects are minimized. The procedure described in Section 2.8 proceeds along these lines. It was applied in [8], but without quantification of the difference it makes or investigation of the requirements for the removed layer thickness. The *oversampling* approach follows the opposite way by using an enlarged sampling block so that the conductivity measured in the domain of interest is not "polluted" by the boundary effects confined in the peripheral region. The [R+P] boundary conditions described in Section 2.5 is an application of this approach. The term "oversampling" is due to [9] but the method was introduced earlier [10] and used under different names by others, such as [11]. It requires a knowledge of what surrounds the investigated domain, which can be available in the situations addressed in [9, 10, 11] where the aim is the coarsening of a detailed large scale permeability field, but not when operating with a tomographic image.

Let us mention for completeness important contributions about the upscaling of the microscale Stokes equations for flows in porous media, which is a mathematically different problem but just as sensitive to the prescibed boundary conditions. The classical BC's are of the same type as those for conduction problems, combining periodicity, Dirichlet and Neumann conditions. Several of them resulting in significantly different predictions are implemented in [12], where the *undersampling* procedure is also used for the identification of a region nearly unaffected by the BC's. Systematic investigations where many kinds of BC's have been applied and compared have also been conducted in [13, 14], including an effective medium approach similar to [E+P] in the following (see Section 2.5).

Thus, a corpus of knowledge exists in the literature but unfortunately, it consists in many disparate comparisons of approaches in particular cases, and whereas the influence of the choice of a procedure and BC's is always pointed out, the differences between predictions are often presented in an illustrative and/or qualitative way. Even the most systematic studies provide general observations and mention some pitfalls but rarely come up with practical recommendations. Thus, someone in search for practical advices for an application is at a loss to find explicit guidance. Of course, at least in the case of tomographic sample images, there is no "right answer" since what lies beyond the sample boundaries is unknown. If two methods yield different results, it generally cannot be claimed that one of them is "right", although it can sometimes be detected that one (or both) of them is wrong, with a quantitative estimate of just how wrong it has to be. Therefore, our work was conducted with several objectives in mind:

- contribute to the knowledge base by a systematic examination of a variety of materials, with quantification of the influence of the boundary conditions, in relation with the parameters of the system (volume fractions, characteristic length scale of the microstructure, contrast of the local conductivities);
- provide quantitative tools for the assessment of the expected level of confidence associated with predictions, and if possible, propose self-diagnosing procedures;
- identify criteria (possibly just rules of thumb), *a priori* or *a posteriori*, for the detection of the risk-situations where serious artifacts can be expected and particular caution is required.

Fullfilling this involves extensive numerical calculations, but also the definition of quantitative indicators for a rigorous analysis of the results. The work was initiated in [1] by treating tomographic images of several kinds of real materials. Phenomenological knowledge was gained from this collection of particular cases, quantitative assessments have been conducted for each of them, and general trends identified. In the present study, synthetic, numerically generated media are used to explore systematically a wider range of morphological parameters, and more general quantitative criteria are obtained.

Sample	p_x (μm)	Block size L	ε	Physical length scale
FS	6.3	512 $p_x \approx$ 128 l_c	0.0692	Correlation exponential decay length, l_c= 4p_x
BS	6.0	500 $p_x \approx$ 77 l_c	0.232	Correlation exponential decay length, l_c= 6.5p_x
PSM	unity	496 p_x = 124 R	0.04 $\sim$ 0.30	Sphere radius R= 4p_x , integral length l_c $\approx$0.4 to 0.6R
TGF	unity	496 p_x = 124 l_c	0.08 $\sim$ 0.25	Correlation exponential decay length, l_c= 4p_x

Table 1: Main sample characteristics : voxel size p_x, computational domain size L in voxels, porosity ε, and a typical scale for their microstructure.

The paper is organised as follows. Section 2 starts with a description of the context and of the investigated samples, which include tomographic images of real materials and synthetic, numerically generated model media. The mathematical problem to be solved is then stated, and a brief description of the numerical solver is provided. The set of BC's considered in the study is introduced and some of their expected artefacts are commented. The procedure to obtain the full effective conductivity tensor is described, from the whole sample or from measurements in inner subdomains (undersampling). Finally, some rigorous quantification tools for the comparative analysis of the results are introduced. The results are presented in Sections 3-5, starting with global indicators such as the mean conductivities, and especially the distances between tensors resulting from different BC's. Then, qualitative comparisons of the local fields are presented in Section 4, which provide a phenomenological picture of the effects of the boundary conditions, and a quantitative analysis of their differences is conducted. Finally, the undersampling approach is illustrated in Section 5 by applications to several examples. A discussion in Section 6 concludes the paper.

2. Context and methods

2.1. Context

The initial motivation for this study stemmed from a practical thermal problem, which explains that when we decided to investigate with some rigour the issue of the BC's influence in finite domains, for the possible benefit of a wide community of colleagues facing the same difficulties, we kept the thermal terminology and refer to "solid" and "gas" phases with conductivities λ_s and λ_g. However, this bears no particular meaning since the following developments apply for any mixture of two components with different conductivities. In particular, when considering Darcy flow in heterogenous media, what is called here "gas" and "solid" can actually correspond to regions with different permeabilities. Furthermore, the ratio λ_s/λ_g can range from very large in thermal applications to very small if λ stands for mass diffusivity or electrical conductivity in a brine saturated porous medium, where the solid phase is nearly (if microporous) or totally impervious. For this reason, a broad range of conductivity contrasts with $10^{-4} \leq \lambda_s/\lambda_g \leq 10^4$ was explored in the materials presented below (see table 2).

Only binary media are considered, containing two phases with constant, isotropic conductivities. Media with continuous variations of the local conductivity could be treated in the same way. Some of the effects would probably be milder, but the general trends are not expected to differ and the methods and quantification tools presented in the following would retain their interest.

2.2. Investigated materials

Tomographic images of real materials and synthetic model media have been investigated. In all cases, the geometry is described by a phase function Z, defined in a $[L_x \times L_y \times L_z]$ array of cubic p_x^3 voxels, equal to 1 in the pores and to 0 in the solid. Two of its statistical moments are of a foremost interest. The first one is the porosity ε which is the volume average $\langle Z \rangle$. The second one is the spatial correlation function $R_Z(\mathbf{u})$ = Covar($Z(\mathbf{x})$, $Z(\mathbf{x}+\mathbf{u})$) / Var(Z). The integral correlation length $l_c = \int_0^\infty R_Z(u)\mathrm{d}u$ (per direction, if R_Z is anisotropic) provides a length scale associated with the microstructure. When $R_Z(\mathbf{u})$ happens to decay exponentially, this l_c is also equal to the decay length. Note that the samples considered here are all cubic, *i.e.*, L_x=L_y=L_z=L.

The tomographic images are rock samples already examined in earlier works, namely a Fontainebleau sandstone (FS), with porosity 0.0692, fully characterized in [15] (Fig.1a), and a Bentheim sandstone (BS), with porosity 0.232, studied in [16] (Fig.1b). In both cases, the correlation function is isotropic and exponentially decaying. Their characteristics are given in table 1. These two samples were already considered in [1], and they are kept here for comparison

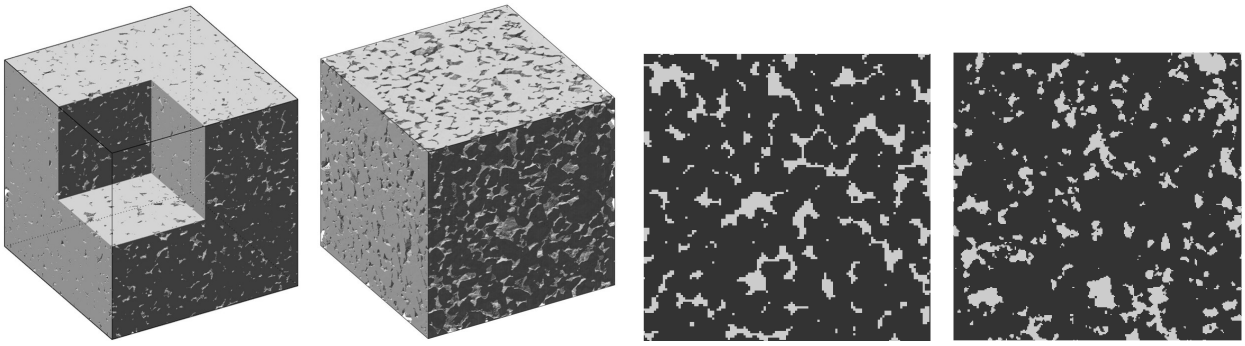

(a) (b) (c) (d)

Figure 1: Samples FS (a) and BS (b). Sections through the model media with ε=0.15: a $[32R]^2$ region in PSM(c); a $[64l_c]^2$ region in TGF (d).

purposes with the synthetic media. The other two samples of [1] were of a different nature, namely thermally degraded polymer-based composites. They were interesting because they are multiscale and anisotropic, but they are not considered here for the sake of concision, and because of their smaller sizes.

Two kinds of model media have been systematically investigated. In the Penetrable Sphere Model (PSM) [15, 16], solid spheres with radius R are inserted with a density ρ, at random positions in the $[128\ R]^3$ unit cell of a periodic medium (Fig.1c). The pore space which remains uncovered has a volume fraction $\varepsilon = \langle Z \rangle = \mathrm{e}^{-\frac{4}{3}\pi R^3 \rho}$. The percolation threshold ε_c of such media is about 0.034. A set of porosities above ε_c has been investigated, with 10 values of ε ranging from 0.04 to 0.30 (see table 2). The spatial correlation is given by eq. (16) in [15]) and the correlation length l_c is about $R/2$ (from $l_c \approx$0.4 R when ε = 0.04 to $l_c \approx$0.6 R when ε = 0.30). Thus the sample size $[128\ R]^3$ roughly corresponds to $[256\ l_c]^3$.

In the Thresholded Gaussian Field (TGF) model [17, 18], a discrete field Z with prescribed mean $\langle Z \rangle = \varepsilon$ and spatial correlation function R_Z is obtained by the following steps. First generate a random uncorrelated Gaussian field X. Convolve it in Fourier space with a kernel derived from the target correlation function R_Z to obtain a correlated Gaussian field Y. Finally, set the phase function Z equal to 1 where Y exceeds a threshold that depends on the target porosity. Here, the correlation was taken isotropic and exponentially decaying according to $R_Z(u) = \mathrm{e}^{-u/l_c}$, and samples of size $[128\ l_c]^3$ were generated (Fig.1d). The percolation threshold ε_c of such media is in the interval 0.08$\sim$0.09. Porosities from this range up to 0.25 have been investigated, (see table 2).

The reconstructed samples are periodic, for both PSM and TGF. The spatial resolution (voxel size) was set to $p_x = l_c/4$ (TGF) or $R/4$ (PSM), so that Z is stored in a $[512]^3$ array. In order to obtain aperiodic samples comparable to tomographic images of real media, a peripheral layer of thickness $2l_c$ or $2R$ is removed from the generated samples, which results in $[124\ l_c]^3$ (for TGF) or $[124\ R]^3$ (for PSM) computation domains. These reduced domains are called Ω whereas the larger initially generated domains are called Ω^+.

2.3. Local and upscaled formulations

Stationary thermal conduction in a heterogeneous medium with position-dependent thermal conductivity λ is governed on the local scale by Fourier's law and a conservation equation

$$\mathbf{q} = -\lambda \nabla T\,, \qquad \nabla \cdot \mathbf{q} = 0 \tag{1}$$

where $\mathbf{q}$ is the heat flux and T is the temperature. If the medium statististical properties are spatially uniform, it can be regarded on a larger scale as an equivalent homogeneous material with effective properties, and in particular with an effective conductivity $\mathbf{\Lambda}$ which relates the locally averaged flux and gradient

$$\langle \mathbf{q} \rangle = -\mathbf{\Lambda} \cdot \langle \nabla T \rangle\,, \qquad \nabla \cdot \langle \mathbf{q} \rangle = 0 \tag{2}$$

Even though the local conductivity is assumed to be isotropic, the medium structure can be anisotropic and therefore the effective coefficient $\mathbf{\Lambda}$ is in general tensorial. If the medium is not strictly homogeneous, (2) still applies with a position-dependent $\mathbf{\Lambda}$ if its characteristics are slowly varying, *i.e.*, on a regional scale much larger than the microscale

of the λ fluctuations. Then, an intermediate scale (the so-called Representative Elementary Volume, REV) smaller than the former and larger than the latter can exist, upon which volume averages of the flux and gradient can be taken. Note that the REV is often defined only as the minimal averaging volume required to damp porosity fluctuations, whereas we are talking here of the averaging volume necessary for a robust estimation of a transport coefficient. Very often, this is a more stringent criterion, for instance close to a percolation threshold when the conductivity contrast is strong. But as illustrated in Section 5, it can also be a milder criterion in the case of a moderate conductivity contrast.

The upscaling from (1) to (2) reduces of course tremendeously the computational effort required for simulations on the field scale, since much coarser volume elements with effective properties can be used. The theoretical background for the homogenization process is classical and not detailed here (see *e.g.*, [18, 19, 20]). Let us just mention that $\mathbf{\Lambda}$ is a symmetric, positive tensor.

This applies to any diffusion-like process governed by mathematically equivalent equations, such as mass diffusion of electrical conduction. Furthermore, whereas creeping fluid flow through a porous medium is governed locally by Stokes equations, a first upscaling step can reduce the flow problem into a homogenized form similar to (1) involving Darcy's law,

$$\overline{\mathbf{v}} = -\frac{1}{\mu}\, k \nabla p\,, \qquad \nabla \cdot \overline{\mathbf{v}} = 0 \tag{3}$$

where $\overline{\mathbf{v}}$ is the seepage velocity, p is the pressure, μ is the fluid viscosity and k is a permeability coefficient. This formulation applies on a scale much larger than the medium microstructure, but the medium can be heretogeneous on a still larger scale which makes k position-dependent. In this case, a second upscaling can be performed to obtain a counterpart of (2) involving an effective permeability tensor $\mathbf{K}$.

2.4. Solution of the local problem

The problem governed by (1) is solved in the domain Ω or Ω^+ subject to various conditions on its boundary $\partial\Omega$ or $\partial\Omega^+$, which are detailed in the next Section 2.5.

The solver is a distant descendant of that presented in [21], where the formulation is described in full details. Equations (1) are discretized in a finite volume formulation, according to the so-called box integration method. T is determined at the vertices of cubic volume elements. The resulting set of linear equations $\mathbf{A} \cdot \mathbf{T} = \mathbf{B}$ is solved by a conjugate gradient method. Iterations are stopped when the global relative residue $\| \mathbf{A} \cdot \mathbf{T} - \mathbf{B} \|$ becomes smaller than $10^{-6} \| \mathbf{B} \|$. This criterion for the global residue translates into a O(10^{-4}) relative accuracy for the components of the predicted mean flux, and to at most 10^{-3} for pointwise temperature, relative to the overall temperature drop. Note that this is much more demanding than the stopping criterion for routine applications, where 10^{-4} is regarded as sufficient. This much finer (and numerically much costlier) accuracy is required for a reliable comparison of the solutions for different BC's. The computation time depends of course on the sample size, but also strongly on the conductivity contrast. For the record, the determination of a conductivity tensor (3 solutions for different mean gradient directions) in FS takes 10$\sim$20h when $\lambda_s/\lambda_g \sim 10^{-1}$ and $\sim$100h when $\lambda_s/\lambda_g \sim 10^{-4}$ (single core 3.4GHz Xeon CPU time; of course, the computations were run in parallel over multiple cores). Since [E+P] is an iterative procedure in an enlarged domain, some calculations took up to 800h. In routine applications, the stated CPU times should be divided by about 10 (resp. O(10^2)) if an accuracy of 0.1% (resp. 1%) for the global conductivity tensor is regarded as sufficient.

The volume averages $\langle \mathbf{q} \rangle$ and $\langle \nabla T \rangle$ of the flux and gradient in Ω are actually evaluated by the surface integrals

$$\langle \mathbf{q} \rangle = \frac{1}{\Omega} \int_{\partial\Omega} \mathbf{q}(\mathbf{x}) \cdot \mathbf{n}\, \mathbf{x}\, \mathrm{d}s\,, \qquad \langle \nabla T \rangle = \frac{1}{\Omega} \int_{\partial\Omega} T \mathbf{n}\, \mathrm{d}s \tag{4}$$

where $\mathbf{n}$ is the unit outwards vector normal to $\partial\Omega$.

2.5. Investigated boundary conditions

A natural way to set the overall BC's for the solution of problem (1) in a finite sample Ω without knowledge of what lies beyond its boundaries $\partial\Omega$ is to mimic real or virtual experimental settings, as illustrated in fig. 2. Permeameter conditions, named after a common apparatus for permeability measurements, correspond to the situation where the sample is placed between two isopotential chambers (Dirichlet conditions) and enclosed transversally in an impervious jacket. Obviously, the no-flux condition through the transverse boundaries constrains the flux directionally and makes

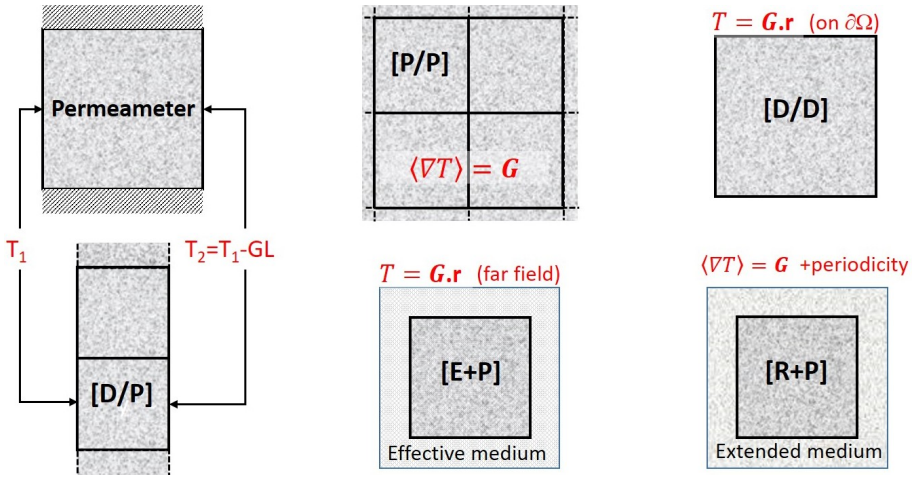

Figure 2: Setups for the real or virtual experiments associated with the boundary conditions described in section 2.5.

this approach inappropriate for the determination of the full tensors $\mathbf{\Lambda}$ or $\mathbf{K}$ in anisotropic media. Therefore, in spite of their frequent use, permeameter conditions have not been included in the set of investigated BC's listed below.

[D/P] The disturbing impervious walls of the permeameter can be removed in a virtual experiment where the single jacketed sample is replaced by a layer of juxtaposed replicas exposed to the same upstream and downstream Dirichlet conditions. We call the corresponding BC's [D/P], standing for "Dirichlet" and "periodic" in the axial and transverse directions, respectively. For instance, for a calculation along the x direction,

$$T(x=0) = GL_x \quad T(x=L_x) = 0 \tag{5a}$$

$$\mathbf{q}_2 = \mathbf{q}_1\,, \quad T_2 = T_1 \qquad \text{at homologous points } (\mathbf{x}_1, \mathbf{x}_2) \text{ on opposite transverse faces of } \partial\Omega \tag{5b}$$

[P/P] In another virtual experiment, the entire space can be covered by such identical replicas. Periodicity of fluxes and temperature gradient can be applied along all directions, regardless of a geometrical mismatch at opposite faces of the sample. If $\mathbf{G}$ is a prescribed macroscopic temperature gradient,

$$\mathbf{q}_2 = \mathbf{q}_1\,, \quad T_2 - T_1 = \mathbf{G}\cdot(\mathbf{x}_2 - \mathbf{x}_1) \quad \text{at homologous points } (\mathbf{x}_1, \mathbf{x}_2) \text{ on any opposite faces of } \partial\Omega \tag{6}$$

[E+P] One may consider that the sample Ω perceives its surroundings as a homogeneous material with the same effective conductivity (to be determined), submitted to far-field conditions in the form of a prescribed macroscopic gradient. A sheath of homogeneous material tentatively screens out most of the influence of the outer BC's and the enlarged domain Ω^+ can be treated as periodic since there is no geometrical mismatches at its boundaries. Thus, problem (1) is solved in Ω^+, with the periodicity conditions (6) applied on $\partial\Omega^+$. We call this [E+P], for "encased" and "periodic". Integrations (4) to obtain the mean flux and gradient are restricted to Ω.

The embedding medium is given an conductivity $\mathbf{\Lambda}_E$, possibly anisotropic, equal to that obtained in Ω. Since the latter is not known beforehand, this is an iterative process. A reasonable guess for $\mathbf{\Lambda}_E$ is used first, which is updated after successive resolutions, until convergence. The layer added on the six faces of the samples was 16 voxels thick for the tomographic images, $2l_c$ for TGF and $2R$ for PSM. It has been checked that this is sufficient to make the results nearly independent of the layer thickness, both for the global parameters and for the local deviations in Ω, by comparison with systematic data for the tomographies with a thickness of 8 voxels, and selected cases for the synthetic media (*e.g.*, with $4l_c$ and $8l_c$ for TGF).

It is worth noting that although the idea of a self-consistent effective medium scheme is very common in theoretical models for the conductivity of composites such as those of Bruggeman [22] or Landauer [23], it seems that its numerical counterpart has not been implemented in earlier works for the upscaling of conduction properties (but it is in [13, 14] for the upscaling of the Stokes flow equations, and in [24] to compute the elastic properties of low-density materials).

[D/D] In a somewhat far-fetched approximation, one may assume that the far-field conditions of [E+P] apply down to $\partial\Omega$. In these so-called "Immersion" conditions, denoted [D/D], Dirichlet conditions are imposed on the entire boundary $\partial\Omega$ of the domain, corresponding to a prescribed mean gradient, with

$$T(\mathbf{x}) = \mathbf{G}\cdot\mathbf{x}\ , \qquad \text{on } \partial\Omega \tag{7}$$

within an arbitrary additive constant. In practice, with $\mathbf{G}$ along one of the axes of coordinates, this results in Dirichlet conditions (5a) on inlet/outlet faces and linear profiles along the transverse faces. Note that a counterpart of [D/D] was considered in [25] where the normal flux instead of T is prescribed on the boundaries, with $\mathbf{q}(\mathbf{x})\cdot\mathbf{n} = \mathbf{B}\cdot\mathbf{n}$ on $\partial\Omega$, where $\mathbf{B}$ is a prescribed vector which correspond to $\langle\mathbf{q}\rangle$, as shown by (4).

[R+P] The last kind of BC's considered here is a special case, applicable only to synthetic media and introduced only for comparison purposes. Recall that periodic PSM and TGF samples Ω^+ with sizes $[128\ l_c]^3$ or $[128\ R]^3$ are generated first, which are subsequently reduced by removal of a peripheral layer to obain aperiodic domains Ω similar to tomographic images (see section 2.2). However, problem (1) can also be solved in Ω^+ with periodicity conditions, as done in [E+P]. Again, integrations (4) to obtain the mean flux and gradient are restricted to Ω. This is akin to the oversampling method [9, 10, 11] where the properties of a sample are determined by solving the flow problem in an wider domain, when the required data are available, *e.g.*, when determining the properties of a block extracted from whole-field data. It is also possible for our numerically generated samples, and provides a "reference" solution (hence the name [R+P]). Note however that Ω is supposedly the only data available. The larger Ω^+ is a periodic continuation of Ω but not the unique possible one and therefore, "reference" does not mean "right" or "unique".

Extensive references are provided in [1] for many applications in the literature of the various BC's mentioned in the above, and of some others. In particular, the computation domain is sometimes made periodic by juxtaposing mirrored images of Ω. This approach was not considered here because as the permeameter conditions, it introduces directional constraints and the eigen-directions of $\mathbf{\Lambda}$ or $\mathbf{K}$ can only be found aligned with the artificial planes of symmetry, as demonstrated for instance in [13, 14].

2.6. Artefacts associated with the boundary conditions

With the exception of [P/P] applied to periodic media, which generally means model media, all the conditions listed in Sec.2.5 present some undesirable features. Consider for illustration purposes the most severe situations where only the pore phase is conducting (λ_s=0). Milder but similar effects are expected for moderate contrasts.

Periodicity [P/P] imposes that the fluxes on opposite faces are equal, but since the phase arrangements in these faces do not match in aperiodic media, the flux has to cross a plane with a much reduced open fraction, equal to ε^2 in the average (Fig. 3a). This introduces a "skin" resistance, and the overall conductivity is underestimated. With Dirichlet conditions [D/P], flux can enter any pore showing on the inlet face of Ω, although some of them are actually dead-ends and would receive no flux from the actual upstream material (Fig. 3b). The overall conductivity is overestimated. With the pressure condition (7) of [D/D], flux can leave or enter any pore showing on a lateral face of Ω, as if some continuous conducting material lay beyond $\partial\Omega$. This creates long-range connections all along the lateral faces (Fig. 3c), which can behave as an apparent lateral conducting skin. The overall conductivity is overestimated. These effects of [D/D] are also illustrated in [13, 14] in the context of fluid flow governed by Stokes equations.

Note that the artefacts associated with [P/P] and [D/P] are local features. They affect the transfers through a surface which the flux has to cross (if $\perp \langle\nabla T\rangle$) or might cross (if $\parallel \langle\nabla T\rangle$). Conversely, the artefact introduced by [D/D] has long range effects generally with stronger impact on the predicted conductivity, as indeed observed in the following. In a caricatured situation, it would yield non-zero flux and effective conductivity if Ω were entirely filled with insulating material except for small unconnected conducting parts located at its corners.

2.7. Determination of a full tensor $\mathbf{\Lambda}$

Equations (1) are solved subject to one of the BC's listed in Sec.2.7, say [BC], with the vector $\mathbf{G}$ set successively along the x-, y- and z-directions. In each case, the mean flux $\langle\boldsymbol{q}\rangle_\xi$ and gradient $\langle\nabla T\rangle_\xi$ (ξ=x, y or z) are evaluated by means of (4). Note that $\langle\nabla T\rangle$ in Ω is equal to $\mathbf{G}$ in the cases of [D/P], [P/P] and [D/D]. However, when $\mathbf{G}$ is applied

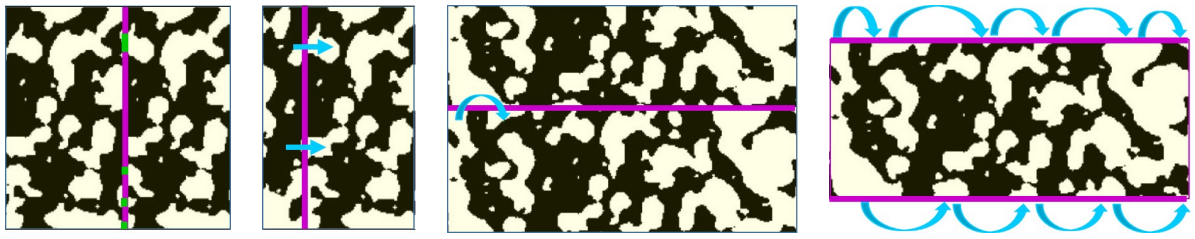

(a) (b) (c) (d)

Figure 3: Artefacts associated with the [P/P], [D/P] and [D/D]. Examples when only the white phase (pores) is conducting. The mean flux is oriented from left to right in all cases. (a) With [P/P], the inlet and outlet faces have a reduced open fraction (in green) due to geometrical mismatch. (b) With [D/P] and [D/D], flux enters all open parts of the inlet face, although some are actually dead-ends (arrows; likewise at the outlet). (c) At transverse boundaries, [P/P] and [D/P] can create links between unconnected pores (arrow), or ignore links which should exist, whereas (d) [D/D] creates long-range connections between all pores showing on a face.

on the boundaries of the enlarged domain Ω^+ for conditions [E+P] and [R+P], the mean gradient in Ω can be different and has to be calculated from the temperature field by application of (4). Then, the following set of 9 linear equations is solved to determine the 9 components of $\mathbf{\Lambda}_{[BC]}$

$$\langle \mathbf{q} \rangle_\xi = -\mathbf{\Lambda}_{[BC]} \cdot \langle \nabla T \rangle_\xi \,, \qquad \xi{=}x, \, y \text{ and } z \tag{8}$$

With conditions [P/P], [D/D], [E+P] and [R+P], the solutions obtained with different vectors $\mathbf{G}$ can be superposed, in view of the linearity of the governing equations. Therefore, the solution for any $\mathbf{G}$ can be obtained by a linear combination of the solutions with $\mathbf{G}$ set along the three axes, and $\mathbf{\Lambda}_{[BC]}$ determined by (8) can be used to predict the mean flux resulting from any mean gradient.

Conversely, the solutions obtained with [D/P] applied along x, y and z cannot be superposed. Thus, the derivation of $\mathbf{\Lambda}_{[D/P]}$ is only formal, and (8) applies only for $\mathbf{G}$ set along x, y or z. Anyway, it is difficult to conceive a numerical experiment where conditions of the type [D/P] would be imposed along a direction oblique relative to a parallelepipedic sample. Note that the same observations apply as well to the permeameter conditions where transverse periodicity is replaced by a no-flux condition. However, this does not preclude $\mathbf{\Lambda}_{[D/P]}$ from bearing information about the sample conductive properties.

The effective tensor $\mathbf{\Lambda}$ should be symmetric, and $\mathbf{\Lambda}_{[P/P]}$ obtained by (8) with periodicity conditions [P/P] is indeed symmetric. The demonstration relies on a reciprocal theorem (see *e.g.*, [18]). The same line of reasoning shows that $\mathbf{\Lambda}_{[D/D]}$ is also symmetric [25]. However, $\mathbf{\Lambda}_{[D/P]}$, $\mathbf{\Lambda}_{[E+P]}$ and $\mathbf{\Lambda}_{[R+P]}$ are not necessarily symmetric, even though periodicity conditions are applied on $\partial\Omega^+$ in the cases of [E+P] and [R+P]. Symmetry would be ensured with [E+P] and [R+P] only if the averages used in (8) were evaluated over $\partial\Omega^+$ instead of $\partial\Omega$.

Asymmetric tensors are defective, and two techniques are widely used to put up with situations where the upscaling procedure yields an asymmetric result. The simplest is to make the tensor symmetric by averaging it with its transpose,

$$\mathbf{\Lambda}_{sym} = \left(\mathbf{\Lambda}_{[BC]} + \mathbf{\Lambda}^t_{[BC]} \right) / 2 \tag{9}$$

Another approach is to supplement (8) with additional equations stating the symmetry of $\mathbf{\Lambda}_{[BC]}$. The system becomes overdetermined, and it has to be solved in some least-square sense. Generally, some residual asymmetry remains which can be eliminated with (9) [6]. Such expedients are necessary for the practical use of $\mathbf{\Lambda}$ in simulation models, but no such step was taken in the present investigation. The purpose is not to cure the asymmetry of $\mathbf{\Lambda}_{[BC]}$, but to quantify it and explore the circumstances of its occurence.

2.8. Undersampling

The fundamental idea underlying the application of upscaled models is the belief that an effective coefficient $\mathbf{\Lambda}$ exists which relates the locally averaged flux and gradient, regardless of the circumstances (*i.e.*, far-field conditions) which induce $\langle \nabla T \rangle$ at the position where (2) is applied. This has been theoretically established in [26], by considering an REV deep within a macroscopic domain V, under the assumption that the macroscale and the REV scale are widely separated. However, whether this requirement is fulfilled in practice in a given sample has to be checked directly, as well as the screening distance and whether an REV remains when the corresponding layer is discarded.

On this premise, it can be attempted to determine this value of $\mathbf{\Lambda}$ by focusing on some inner subdomain Ω_c in Ω. If the tensor $\mathbf{\Lambda}_c$ obtained by (8) with the mean fluxes and gradients given by the integrals (4) applied to Ω_c is found independent of the conditions applied at $\partial\Omega$, this $\mathbf{\Lambda}$ fulfills the aforementioned requirement for its use in upscaled models. This methodology has been applied in [8] for conduction processes, and in [12] for fluid flow.

We have applied this approach with subdomains $\Omega_c(M)$ obtained by removing from Ω a peripheral layer with thickness M. The conductivity tensor of Ω_c obtained from the solution of (1) with conditions [BC] at $\partial\Omega$ is denoted $\mathbf{\Lambda}_{[BC],c}(M)$. Obviously, a thick enough margin (M not too small) is required to screen out the influence of the outer conditions. On the other hand, the subvolume Ω_c has to be sufficient (M not too large) to remain representative, *i.e.*, to prevent the occurence of large statistical fluctuations. If the whole sample Ω is large enough, an intermediate range for M can exist where both of these criteria are fulfilled. This means that over this interval, $\mathbf{\Lambda}_{[BC],c}(M)$ should be independent of [BC] (first criterion) and M (second criterion), *i.e.*, the effective tensor $\mathbf{\Lambda}$ for the investigated material.

Of course, the term "independent" has to be understood within some practical tolerance, and a quantitative indicator is required to measure the difference between two tensors. Such an indicator is defined in Sec.2.9.

2.9. Notations and quantification tools

A few notations and definitions are introduced here, which are used in the subsequent discussions. First, the mean $\overline{\Lambda}$ of the diagonal terms of a tensor $\mathbf{\Lambda}$, the anisotropy index $\mathscr{N}$, the arithmetic and harmonic volume averages of the local conductivities $\langle\lambda\rangle$ and $\langle\lambda\rangle_H$ and the index τ are defined by

$$\overline{\Lambda}=\frac{1}{3}\sum_i \Lambda_{ii}\,,\qquad \mathscr{N}=\frac{\Lambda_{max}}{\Lambda_{min}}\,,\qquad \langle\lambda\rangle=\frac{1}{\Omega}\int_\Omega \lambda\,\mathrm{d}v\,,\qquad \langle\lambda\rangle_H^{-1}=\frac{1}{\Omega}\int_\Omega \lambda^{-1}\,\mathrm{d}v\,,\qquad \tau=\frac{\langle\lambda\rangle}{\Lambda_{min}}-1 \tag{10}$$

where Λ_{max} and Λ_{min} are the largest and smallest eigenvalues of $\mathbf{\Lambda}$. $\langle\lambda\rangle$ and $\langle\lambda\rangle_H$ are the fully general upper and lower Wiener's bounds. In addition, Hashin & Shtrikman's upper and lower bounds [27] are denoted by Λ^U_{HS} and Λ^L_{HS}. Both sets of bounds only depend on the phase conductivities and volume fractions, but the tighter Hashin & Shtrikman's bounds apply only to isotropic media. The index τ discriminates situations where the volume containing the most conducting phase is well connected (Λ=O($\langle\lambda\rangle$), $\tau\lesssim 1$), or tortuous and/or poorly connected ($\Lambda\ll\langle\lambda\rangle$, $\tau\gg 1$). For the nearly isotropic media considered here, Λ_{min} in the definition of τ is close to $\overline{\Lambda}$, but it is very different for some anisotropic materials considered in [1].

A distance is introduced to quantify the difference between two tensors, say $\mathbf{\Lambda}_1$ and $\mathbf{\Lambda}_2$, resulting for instance from different upscaling protocols. In response to a same unit gradient $\boldsymbol{g}$, these tensors predict fluxes $\boldsymbol{q}_i=-\mathbf{\Lambda}_i\cdot\boldsymbol{g}$. The squared norm of their deviation $\|\,\boldsymbol{q}_2-\boldsymbol{q}_1\,\|^2$ is equal to $\boldsymbol{g}^t\cdot(\mathbf{\Lambda}_2-\mathbf{\Lambda}_1)^t\cdot(\mathbf{\Lambda}_2-\mathbf{\Lambda}_1)\cdot\boldsymbol{g}$. It is maximum when $\boldsymbol{g}$ is aligned with the eigendirection of $(\mathbf{\Lambda}_2-\mathbf{\Lambda}_1)^t\cdot(\mathbf{\Lambda}_2-\mathbf{\Lambda}_1)$ associated with its largest eigenvalue. Therefore, we measure the difference of $\mathbf{\Lambda}_1$ and $\mathbf{\Lambda}_2$ by the distance $\mathscr{D}$ and the normalized dimensionless quantity $\mathscr{D}'$ defined by

$$\mathscr{D}^2(\mathbf{\Lambda}_1,\mathbf{\Lambda}_2)=\text{largest eigenvalue of }\left[(\mathbf{\Lambda}_2-\mathbf{\Lambda}_1)^t\cdot(\mathbf{\Lambda}_2-\mathbf{\Lambda}_1)\right],\quad \mathscr{D}'=\frac{\mathscr{D}}{\left[\overline{\Lambda_1}\;\overline{\Lambda_2}\right]^{1/2}} \tag{11}$$

$\mathscr{D}'(\mathbf{\Lambda}_1,\mathbf{\Lambda}_2)$ is the maximal relative deviation (combining magnitude and direction differences) of the fluxes predicted by $\mathbf{\Lambda}_1$ and $\mathbf{\Lambda}_2$ when applied to the same gradient. Note that the $\mathbf{\Lambda}_i$'s do not need to be symmetric in the definition (11), and that $\mathscr{D}$ is a distance in the mathematical sense, *i.e.*, a symmetric positive-definite function satisfying the triangle inequality. Although $\mathscr{D}$ is used in other contexts to measure the difference between matrices (to monitor the convergence of iterative numerical schemes [28]) we are not aware of its use for the comparison of tensorial transport coefficients prior to [1].

Another quantity of interest is the asymmetry index $\mathscr{A}$ and its normalized dimensionless counterpart $\mathscr{A}'$,

$$\mathscr{A}^2(\mathbf{\Lambda})=\sum_{1\le i<j\le 3}\left[(\Lambda_{ij}-\Lambda_{ji})/2\right]^2\,,\qquad \mathscr{A}'(\mathbf{\Lambda})=\mathscr{A}(\mathbf{\Lambda})/\overline{\Lambda} \tag{12}$$

This indicator has an interesting relation with $\mathscr{D}$, namely that if $\mathbf{\Lambda}_2-\mathbf{\Lambda}_1$ is antisymmetric, then $\mathscr{D}(\mathbf{\Lambda}_1,\mathbf{\Lambda}_2)=\mathscr{A}(\mathbf{\Lambda}_2-\mathbf{\Lambda}_1)$. This implies that if a tensor $\mathbf{\Lambda}_{[BC]}$ resulting from an upscaling procedure is not symmetric, it differs from $\mathbf{\Lambda}_{sym}$ obtained by the symmetrization (9) by $\mathscr{D}\left(\mathbf{\Lambda}_{[BC]},\mathbf{\Lambda}_{sym}\right)=\mathscr{A}\left(\mathbf{\Lambda}_{[BC]}\right)$, and by *at least* that much from any possible acceptable (and therefore symmetric) conductivity tensor. Furthermore, this is only a lower bound for

the error. For instance, say $\mathbf{\Lambda}_{[BC]}$ differs from an exact value $\Lambda \boldsymbol{I}$ by a Gaussian noise with standard deviation $\sigma\Lambda$ for all its components.Then $\langle \mathscr{A}' \left(\mathbf{\Lambda}_{[BC]}\right)\rangle \approx 0.33\sigma$ and $\langle \mathscr{D}' \left(\mathbf{\Lambda}_{[BC]}, \Lambda \boldsymbol{I}\right)\rangle \approx 4.9 \langle \mathscr{A}' \rangle$ (averages over 10^8 Monte Carlo realizations). Hence, even a moderate asymmetry by a few percent should be considered with attention instead of carelessly eliminating it with (9), since it can point at a quite significant uncertainty in the tensor determination.

2.10. Notes about the influence of the spatial resolution

The discrete representation of a medium and the predicted fluxes (and therefore conductivity tensor) obtained when solving (1) obviously depend on the spatial resolution, and possibly on preliminary treatments of the primary tomographic or geophysical data. In particular, singular contacts can be overlooked, or near-contacts can be interpreted as actual contacts, with significant impact when the property contrast is large, whatever the BC's. These effects have been examined in details in [29, 30]. However, while singular contacts (or lack of) make a difference for the fields in a region around them, they do not affect the thickness of the peripheral layer where the kind of BC's is felt, unless the property contrast is extreme and a very coarse resolution prevents the conducting phase from percolating; but then sensitivity to the BC's becomes a secondary issue.

Sensitivity to spatial resolution and to the boundary conditions both contribute to the uncertainty of the conductivity prediction, but they are different and mostly independent matters. We focus in the present work on the latter, which remains even if the resolution is excellent, and on the way to get the best out of an available digital image. If need be, the proposed procedures can be applied to variants of the image resulting from different pre-treatments.

Furthermore, the trends and general observations mentioned in the following regarding the differences between predictions from different BC's are not expected to depend on resolution. This is supported by the similarity of the observations for the present samples, whose resolution quantified by the ratio l_c/p_x ranges from 1.6 to 6.5 (see table 1), and by a direct comparison for model media (not reported here). For instance, identical $[64\ R]^3$ PSM samples have been discretized with R=4, 6 and $8p_x$. The responses to different BC's differ in the same way in all cases, over the whole range of porosity and conductivity contrast.

2.11. Summary of the investigated cases

The combinations of porosities, conductivity contrast and boundary conditions considered for the various kinds of samples are summarized in table 2. Twenty-four values of λ_s/λ_g ranging from 10^{-4} to 10^4 have been used in FS and BS, for all BC's described in section 2.5 except [R+P], by lack of data in the surroundings of the samples. Note however that the undersampling technique is a way to reach the same objective.

Several values of the porosities have been considered in the model media, up to 0.25 (TGF) and 0.30 (PSM). Since the results for FS and BS show that nothing dramatic occurs when the most conducting phase is also the most present, the range of contrast was reduced in the model media with $10^{-4} \leq \lambda_s/\lambda_g \leq 10^{-1}$, *i.e.*, the cases when the least present phase (pores) is the most conducting. All BC's but [D/D] have been applied in TGF, and all but [E+P] in PSM, except for the cases indicated in table 2 where the 5 kinds BC's were imposed.

Four stochastic realizations have been treated in each case for the model media. Unless otherwise stated, the results presented in the following are averages over the four samples. These averages are arithmetic for quantities such as $\overline{\Lambda}$ and quadratic (RMS) when deviations such as $\mathscr{D}'$ or $\widetilde{\delta T}$ in section 4, are considered.

3. Results for Global Indicators

We consider here global indicators, *i.e.*, quantities which can be deduced from the tensors $\mathbf{\Lambda}$ obtained by solving problem (1) subject to with the various BC's without scrutinizing the local fields.

The simplest one is the mean conductivity $\overline{\Lambda}$, which is plotted as a function of λ_s/λ_g in Fig.5, for FS, BS and examples of PSM and TGF with porosities 0.08 and 0.12, and for all investigated BC's. The graphic conventions for this figure and subsequent ones are explicited in Fig. 4. $\overline{\Lambda}$ is normalized by $\langle\lambda\rangle$ for an easier comparison of results with very different orders of magnitude when the phase conductivities vary. Note that the ratio $\overline{\Lambda}/\langle\lambda\rangle$ can be viewed as a tortuosity factor, since it approaches one when most heat flow takes place along straight streamlines in the most conducting phase. The samples are actually slightly anisotropic. The anisotropy index $\mathscr{N}$ (see eq. 10) can reach about 1.2 in FS and in individual realizations of PSM (with large contrasts and small porosities), 1.16 in BS and 1.08 in PSM, but plots of Λ_{min} and Λ_{max} look very similar to Fig.5. Several general features stand out, whatever the BC's.

λ_s/λ_g	FS (ε=0.0692) and BS (ε=0.232)
10^{-4}	[B]
...	[B]
10^{+4}	[B]
(24 values of λ_s/λ_g, see Fig.4a)	

	TGF, with ε=					
λ_s/λ_g	0.08	0.10	0.12	0.15	0.20	0.25
10^{-4}	[C]	[C]	[C]	[C]	[C]	[C]
10^{-3}	[C]	[C]	[C]	[C]	[C]	[C]
10^{-2}	[C]	[C]	[C]	[C]	[C]	[C]
10^{-1}	[C]	[C]	[C]	[C]	[C]	[C]

	PSM, with ε=									
λ_s/λ_g	0.04	0.05	0.06	0.07	0.08	0.10	0.15	0.20	0.25	0.30
10^{-4}	[D]		[D]		[D]		[D]		[D]	
10^{-3}	[A]	[D]	[A]	[D]	[A]	[D]	[A]	[D]	[A]	[D]
10^{-2}	[D]		[D]		[D]		[D]		[D]	
10^{-1}	[D]		[D]		[D]		[D]		[D]	

	A	B	C	D
[D/P]	x	x	x	x
[P/P]	x	x	x	x
[D/D]	x	x		x
[E+P]	x	x	x	
[R+P]	x		x	x

Table 2: Investigated cases for the tomographic images and model materials. The sets [A]-[D] of BC's are defined in the bottom-right table.

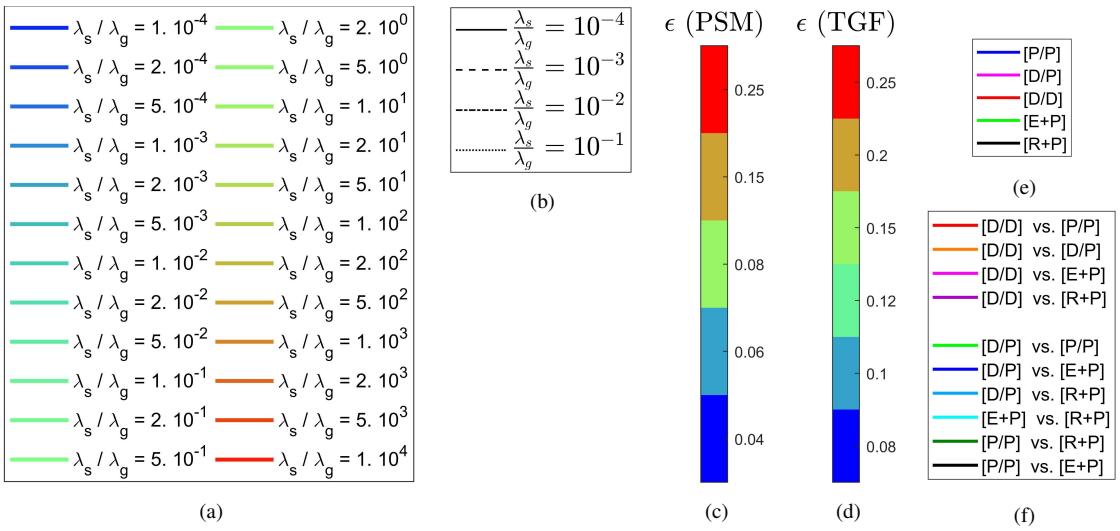

Figure 4: Line type and color conventions used in subsequent figures.

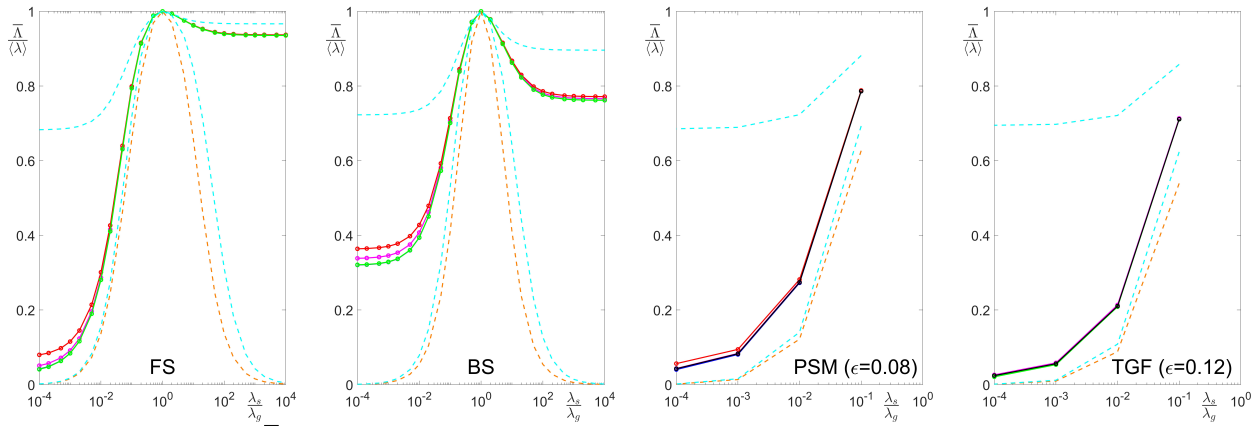

Figure 5: Mean conductivity $\overline{\Lambda}$ normalized by $\langle\lambda\rangle$ as a function of λ_s/λ_g, obtained by applying various BC's (color code as shown in Fig.4e). Hashin & Shtrikman's bounds (broken blue lines) and Wiener's lower bound $\langle\lambda\rangle_H$ (broken orange lines) are also shown for comparison.

(a) When the conductivity contrast is very large, one expects that one of the phases ultimately plays a negligible role, and that an infinite ratio or some very large finite value makes vanishing difference. This is observed in many cases, with established asymptotical values beyond $10^{\pm 3}$, but $\overline{\Lambda}/\langle\lambda\rangle$ is still decaying when $\lambda_s/\lambda_g \sim 10^{-4}$ in some others. It has been checked that the gas space is percolating in all these cases, which implies that some non-zero asymptotic value exists when $\lambda_s/\lambda_g \to 0$, but convergence is not reached in the investigated range. Note that the slow convergences occur when $\overline{\Lambda}/\langle\lambda\rangle$ is small, *i.e.*, when $\tau \gg 1$.

(b) For comparison, Wiener's lower bound $\langle\lambda\rangle_H$ and Hashin & Shtrikman's bounds Λ^L_{HS} and Λ^U_{HS} are also shown in Fig.5 (Wiener's upper bound corresponds to unity). Of course, all these bounds provide reasonable estimates for small contrasts, but they grossly deviate from the numerical data for λ_s/λ_g beyond $10^{\pm 1}$. Note that the eigenvalues of $\mathbf{\Lambda}$ sometimes slightly exceed the Hashin & Shtrikman's bounds. This is not aberrant, since Hashin & Shtrikman's bounds apply to isotropic media and do not constrain Λ_{Max} and Λ_{Min} in anisotropic ones.

(c) Solid is largely predominant in FS and BS. Therefore, when it is the most conducting phase, tortuosity is minimal and $\overline{\Lambda}$ is not much smaller than $\langle\lambda\rangle$. In the opposite case of $\lambda_s \ll \lambda_g$, $\overline{\Lambda}/\langle\lambda\rangle \sim 1/20$ (FS) or 1/3 (BS).

(d) Even though ε=0.12 for the example of TGF is larger that the porosity in FS (0.069) or in the example of PSM (0.08), its ratio $\overline{\Lambda}/\langle\lambda\rangle$ is smaller when solid becomes nearly insulating. This results from a poor connectivity of the pore space: 0.12 is not much larger than the percolation threshold $\varepsilon_c \sim 0.09$ of TGF, while 0.08 is more than twice $\varepsilon_c \approx 0.034$ for PSM. Similar and more dramatic illustrations of the influence of the morphology can be found in [1], in foam-like media where porosity is large but the pores consist in poorly connected inclusions.

The volume fraction and connectivity issues mentioned in (c,d) are expected to influence the impact of the BC's on the determination of $\mathbf{\Lambda}$. When the most conducting phase is predominant and well connected, artefacts such as those illustrated in Fig.3(a,b) are expected to be minimized. Conversely, strong effects are probable when a poorly connected phase with low volume fraction is the most conducting. The comparison of the data in Fig.5 confirms these expectations. The relative deviations between the predictions from various BC's are small when $\overline{\Lambda} \sim \langle\lambda\rangle$ (*i.e.*, $\tau \lesssim 1$) and large when $\overline{\Lambda} \ll \langle\lambda\rangle$ (*i.e.*, $\tau \gg 1$).

It is also observed that the predictions of [P/P], [R+P] and [E+P] are generally in fair agreement, that those of [D/P] somewhat deviates from them, and that [D/D] can yield very different and always larger results. This can be quantified and analyzed in more details by considering a secong global indicator, namely the relative difference $\mathscr{D}'$ between tensors resulting from calculations with different BC's. Furthermore, beyond the mere difference in mean conductivity $\overline{\Lambda}$, the measure $\mathscr{D}'$ incorporates the differences between the eigenvalues as well as the deviations between the eigenvectors of the tensors.

The distance $\mathscr{D}'(\mathbf{\Lambda}_1, \mathbf{\Lambda}_2)$ between the conductivity tensors resulting from calculations with different conditions [BC_1] and [BC_2] is plotted in the top row of Fig.6 as a function of λ_s/λ_g, for the same media as in Fig.5. Note that the very small values of $\mathscr{D}'$ must not be taken literally. The deviations between very similar predictions of $\mathbf{\Lambda}$ for two kinds of BC's involve the influence of the BC's but also the accuracy of the numerical solution of problem (1). Thus, values of $\mathscr{D}' \lesssim 10^{-3}$ are mostly indicative, with the meaning "undistinguishable from a practical point of view".

The hierachy of the curves for the various pairs of BC's complies with what could be perceived in Fig.5. It is clear in particular that the set of curves for the comparions of BC's among [D/P], [P/P], [E+P] and [R+P] (cool bluish colors, see table 4f) is always below the set of curves for comparisons of [D/D] with the other BC's (warm reddish colors). This means that $\mathbf{\Lambda}$ obtained with [D/D] strongly departs from the $\mathbf{\Lambda}$'s resulting from all other BC's, which are in better mutual agreements.

Unsurprisingly, the distance $\mathscr{D}'$ between the predictions increases with the contrast in the conductivities of the components, and reaches asymptotes when the contrast is large. This convergence is achieved or not in the investigated range of λ_s/λ_g in the same cases as the convergence of $\overline{\Lambda}$ in Fig.5. Furthermore, the asymptotic values are clearly in relation with the mean conductivity. When the solid is the most conducting phase in FS and BS, *i.e.* when conduction takes place mostly in the predominant phase and is not strongly impaired by tortuosity as noted in feature (c) in the above, $\mathscr{D}'$ remains small: $O(10^{-3})$ in FS where $\overline{\Lambda}/\langle\lambda\rangle \approx 0.93$, and $O(10^{-2})$ in BS where $\overline{\Lambda}/\langle\lambda\rangle \approx 0.77$. No significant influence of the BC's is to be feared. More concerning values are observed in BS when gas is the conducting phase, with $\mathscr{D}' = O(10^{-1})$ while $\overline{\Lambda}/\langle\lambda\rangle \sim 1/3$. Finally, $\mathscr{D}'$ alarmingly approaches O(1) in all cases where $\overline{\Lambda}/\langle\lambda\rangle \ll 1$.

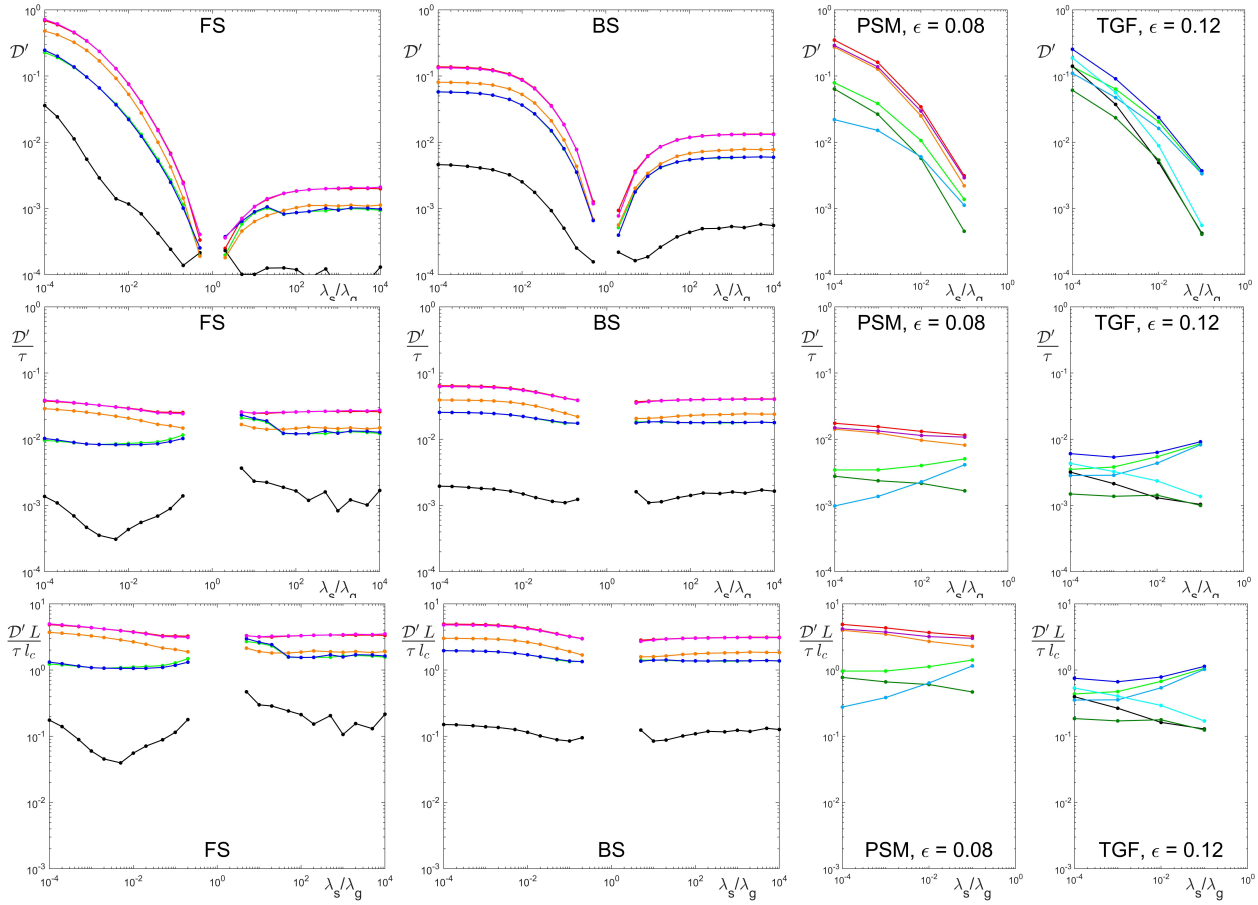

Figure 6: The distance $\mathscr{D}'(\mathbf{\Lambda}_1, \mathbf{\Lambda}_2)$ as a function of λ_s/λ_g. Raw value (top row) and $\mathscr{D}'$ normalized by τ (middle) and by $\tau l_c/L$ (bottom), in FS, BS, PSM (ε=0.08) and TGF (ε=0.12), from left to right. Colors correspond to the pairs of BC's with the convention in Fig.4f.

This anticorrelation of $\mathscr{D}'$ with $\overline{\Lambda}/\langle\lambda\rangle$, or its correlation with τ as defined in (10), is checked directly by the plots of $\mathscr{D}'/\tau$ in the second row of Fig.6. This strickingly levels the results. The variations of $\mathscr{D}'$ which span 2 or 3 orders of magnitude when λ_s/λ_g varies are reduced to a factor $\lesssim$2 for the corresponding curves for $\mathscr{D}'/\tau$ (recall that the very small values of $\mathscr{D}'$ should only be regarded as indicative). For instance, the two very different asymptotes of $\mathscr{D}'$ on either sides of the curves in FS yield very similar ratios $\mathscr{D}'/\tau$.

In addition, it is expected that the sensitivity to the BC's depends on the sample size, since its originates in disturbances near the sample boundaries which gradually decrease deeper in its volume. This size has to be measured relative to the characteristic scale of the material texture, which we quantify here by the correlation length l_c. Therefore, the same data for $\mathscr{D}'$ are plotted again in the bottom row of Fig.6, normalized by $\tau l_c/L$. The shapes of the curves are of course the same as for $\mathscr{D}'/\tau$, but this additional normalization shifts them vertically and bring them at similar levels. Relative to FS and TGF which both have sizes $L/l_c \approx$128, the curves for BS ($L/l_c \approx$77) are shifted downwards and those for PSM ($L/l_c \approx$280) are shifted upwards.

Figure 7 where $\mathscr{D}' L/l_c$ is plotted as a function of τ illustrates this in a systematic way. The data from all our calculations are presented, including all ratios λ_s/λ_g, in FS, BS and all the individual realizations of the synthetic media PSM and TGF, for all the values of their porosities and for all pairs of BC's. Additionnal data obtained in [1] for tomographic images of other anisotropic, multiscale materials are also shown. This amounts to about 1500+300 data points, though many of them overlap and cannot be distinguished in this loglog plot. An upper envelope is clearly visible, which corresponds to

$$\mathscr{D}' \lesssim 5\,\tau\,\frac{l_c}{L} = 5\left[\frac{\langle\lambda\rangle}{\Lambda_{min}} - 1\right]\frac{l_c}{L} \tag{13a}$$

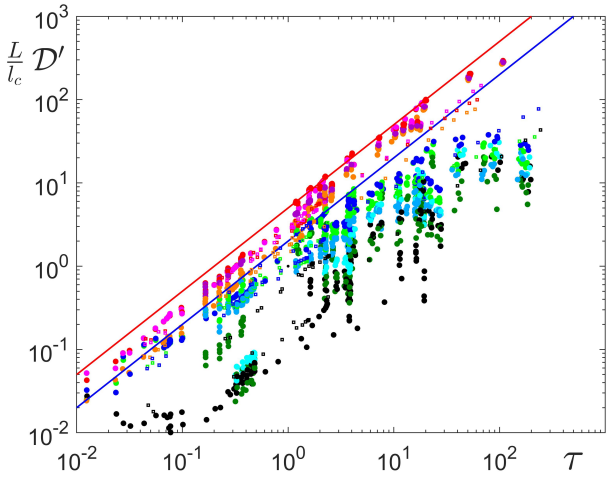

Figure 7: The normalized difference $\mathscr{D}'(\mathbf{\Lambda}_1,\mathbf{\Lambda}_2)L/l_c$ as a function of τ. The data for all ratios λ_s/λ_g in FS, BS and all the individual realizations of the synthetic media PSM and TGF for all the values of their porosities and for all pairs of BC's are included. Colors correspond to the pair of BC's with the convention in Fig.4f. Small dots are additional data obtained in [1] for tomographic images of other anisotropic, multiscale materials. Solid lines correspond to 2τ (blue) and 5τ (red).

All the data are below this limit, and deviations $\mathscr{D}'$ which approach this limit are observed for all the media/conductivity contrast combinations, for some pair of BC's. In practice, this pair always involves [D/D]. The corresponding points (reddish colors) are all situated in an upper strip, between (13a) and another line which is an upper envelope for $\mathscr{D}'$ when comparing the predictions of $\mathbf{\Lambda}$ resulting from all BC's except [D/D],

$$\mathscr{D}' \lesssim 2\,\tau\,\frac{l_c}{L} = 2\left[\frac{\langle\lambda\rangle}{\Lambda_{min}} - 1\right]\frac{l_c}{L} \qquad \text{([D/D] excluced)} \tag{13b}$$

4. Comparison of local fields

Comparing $\mathbf{\Lambda}_{[BC_1]}$ and $\mathbf{\Lambda}_{[BC_2]}$ resulting from different BC's means comparing the fluxes obtained for an identical $\langle\nabla T\rangle$. From a reversed point of view, the temperature fields corresponding to different BC's but identical mean fluxes can be compared. To this end, the fields obtained when solving problem (1) with unit gradients $\langle\nabla T\rangle$ have been renormalized by the corresponding diagonal component of $\mathbf{\Lambda}$ so that the mean flux component in the direction of $\langle\nabla T\rangle$ is the same for all BC's. Two such fields can be meaningfully compared, and their difference $\widetilde{\delta T}_{[BC_1],[BC_2]}$ is made dimensionless by dividing it by the overall drop ΔT over the whole sample.

Examples are displayed in Fig.8 in a cross-section of a PSM sample with ε=0.08, when λ_s/λ_g=10^{-3}. Large deviations between the fields for [D/P] and [P/P] reaching nearly 10% of ΔT are observed in (a) near the inlet and outlet faces, as expected since this is where the BC's differ (periodicity or Dirichlet). Conversely, no difference is observed along the transverse boundaries, where the BC's are identical. The comparison of [D/P] with [E+P] in (b) shows a similar pattern at the inlet and outlet faces, and also some differences along the transverse boundaries, but of a much smaller amplitude, exceeding 1% of ΔT only a a few spots. In both cases, the two compared fields are nearly identical in a broad central region, where the darkest blue color corresponds to $\widetilde{\delta T} \leq 10^{-3}$.

However, the comparison of [D/P] with [D/D] in Fig.8c (as well as the confrontations of [D/D] with [P/P] and [E+P], not shown) is quite different. Instead of an agreement in a central part and deviations near the boundraies, $\widetilde{\delta T}$ follows a linear trend across the whole sample. This results from the artefact associated with [D/D], discussed in Sec.2.6 and illustrated in Fig.3d. The apparent conducting skin along the transverse boundaries provides an additional path for the heat flux. Therefore, the immersion conditions increase the effective conductivity, as noted in Sec.3. However, the overall mean flux is not representative of the flux in the bulk of the sample, and consequently, after calibration of the T-field, the mean gradient in the bulk does not correspond to a unit mean flux. As a result, the good agreements of the fields in the central regions of Figs.8a,b is replaced by the difference of two different linear trends.

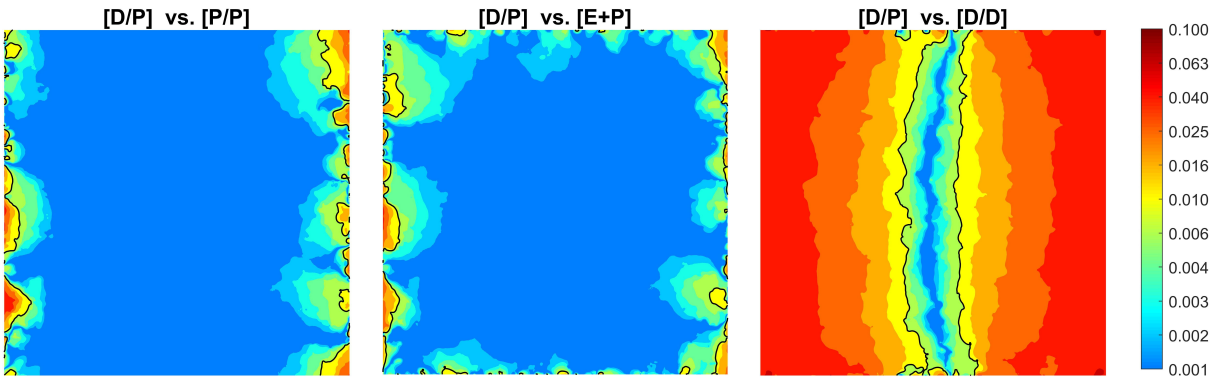

Figure 8: Comparason of local fields in a $[124R]^2$ section of a sample of PSM with ε=0.08. The mean gradient is horizontal and λ_s/λ_g=10^{-3}. Maps of $|\widetilde{\delta T}|$ for BC's [D/P] vs. [P/P] (a), vs. [E+P] (b) and vs. [D/D] (c), in logscale. The black lines corresponds to 10^{-2}.

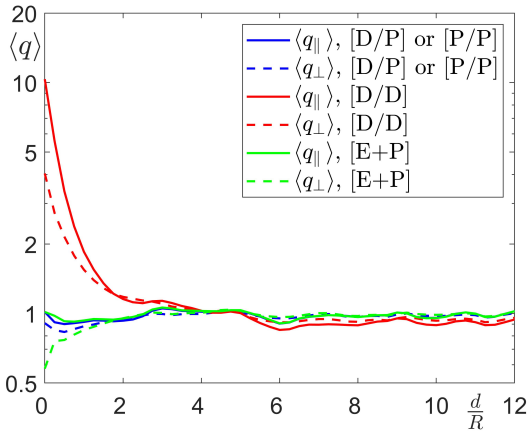

Figure 9: The normalized averages $\langle q_\parallel \rangle$ and $\langle q_\perp \rangle$ as funtions of the distance d/R from the transverse boundaries, for the same sample as in Fig.8.

In order to directly exhibit the conducting skin along the transverse boundaries with [D/D], the local flux field $\boldsymbol{q}$ was recorded in the same case as for Fig. 8. Its component along $\langle \nabla T \rangle$ is denoted by $q_\parallel$ and the norm of its transverse component by $q_\perp$. Their averages $\langle q_\parallel \rangle$ and $\langle q_\perp \rangle$ were measured over planes parallel at a distance d to the transverse boundaries, excluding a $16R$ thick layer near the inlet and outlet, and normalized by the overall averages of $q_\parallel$ and $q_\perp$.

These quantities are plotted in Fig.9 as functions of the distance d/R. With BC's [D/P] or [P/P], both averages remain close to unity, down to $d \to 0$. [D/P] and [P/P] yield the same result, since the fields are identical (see Fig. 8a). With [E+P], $\langle q_\perp \rangle$ drops slightly very close to the boundary, but $\langle q_\parallel \rangle$ remains close to one, and actually nearly identical to that for [P/P] over the whole range of d. Conversely, with [D/D], $\langle q_\parallel \rangle$ sharply increases at distance $d \lesssim 2R$, and exceeds 10 at d=0. This is due to exchanges across the sample boundaries where T is prescribed and accordingly, $\langle q_\perp \rangle$ strongly increases as well. Since the data are normalized by the overall volume average, the excess flux in the peripheral skin is compensated by $\langle q_\parallel \rangle < 1$ in the bulk of the sample. Similar evidence of this [D/D] artefact is visible in Fig.12, as discussed in Section 5.

A detailed and more quantitative anaylsis of the T-fields differences was conducted by considering the profiles along the direction of $\langle \nabla T \rangle$ of the RMS average $\langle \widetilde{\delta T} \rangle_2$. The results are shown here only for the comparison of [D/P] vs. [P/P], which differ only by the inlet/outlet conditions. Therefore the profiles provide a clear view of the affected regions near the upstream and downstream domain boundaries and of the unaffected central region. The latter is blurred in comparisons involving [E+P] and [R+P] because of the differences along the transverse boundaries (see Fig.8b), but if a peripheral layer is filtered out, the resulting profiles are similar to those obtained with [D/P] vs. [P/P]. Of course, a comparison in these terms of [D/D] with other BC's is meaningless, since it only shows the difference in

mean gradient visible in Fig.8c.

The profiles of $\langle\widetilde{\delta T}\rangle_2$ are plotted in Fig.10, for all investigated samples. The raw data in the left column include all the numerical results. In all cases, $\langle\widetilde{\delta T}\rangle_2$ decreases by a factor at least 10 from the boundaries to the central region. The various curves for each kind of material are similar, but spread over about two orders of magnitude, according to the values of ε (in PSM and TGF) and λ_s/λ_g (all materials).

Unsurprisingly, the lowest curves correspond to moderate conductivity contrasts (green curves). Large contrasts yield larger $\langle\widetilde{\delta T}\rangle_2$, by a significant factor when the most conducting phase is the most present (red curves), and by a very large factor when it is the least present (blue curves). This is most easily seen for FS and BS, but the same trend applies in PSM and TGF, though it is less visible because many curves for different porosities are mixed.

This is the same hierarchy as for the global indicator $\mathscr{D}'$ in Fig.6, and a rationalization based on the same parameters τ and l_c/L can be attempted. In the middle column of Fig.10, $\langle\widetilde{\delta T}\rangle_2$ is normalized by $\sqrt{\tau}l_c/L$. The vertical spread of the profiles is very much reduced, spanning a factor of about 2 only for each kind of material. The maximal values at the boundaries are all between 1 and 2, except for a few cases with $\lambda_s/\lambda_g \ll 1$ in FS where it approaches 3. Note that this unification involves $\sqrt{\tau}$ instead of τ in the normalization factor for $\mathscr{D}'$ in Fig.6 and eq. 13.

Another normalization is made in the right column of Fig.10, where $\langle\widetilde{\delta T}\rangle_2$ is simply divided in each case by its value at the boundaries. This is even more successful in gathering the various curves, mostly because it eliminates the spread of the end values, and it demonstrates that all the profiles for each kind of media have the same shape.

There is a little cheat in the normalized profiles in Fig.10 (middle and right columns): a few cases have been omitted, namely (λ_s/λ_g=10^{-4}, $\varepsilon \leq$0.15) for TGF and (λ_s/λ_g=10^{-4}, $\varepsilon \leq$0.08) and (λ_s/λ_g=10^{-3}, ε=0.04) for PSM. Atypical profiles are observed in these situations of a small amount of conducting gas in a nearly insulating solid.

These data are included in Fig.11, where the decay of the RMS deviation $\langle\widetilde{\delta T}\rangle_2$ is shown for all kinds of material together, as a function of the distance x from the inlet/outlet faces, normalized by their correlation length l_c. However, another selection has been applied, with two families of situations: first, data for the low-porosity FS (ε=0.069) sample and those for the aforementioned low-porosity synthetic media with extreme contrasts (red curves); second, data for BS (ε=0.232) and most data for the synthetic media, excluding those with small porosity or extreme conductivity contrasts, *i..e.*, retaining only the cases where proximity to a percolation threshold is certainly not an issue (blue curves). The curves for these two families are clearly gathered in two separate groups. Only a few cases of synthetic media on the fringe between them yield profiles intermediate between the two groups, such as PSM (ε =0.08) and TGF (ε =0.15) with $\lambda_s/\lambda_g = 10^{-3}$ (green curves), which are the examples used in Figs.6, 8, 12, and 13.

Hence, while $\langle\widetilde{\delta T}\rangle_2$ at $x = 0$ scales approximately as $\sqrt{\tau}l_c/L$, its decay length within the material does not only depend on the textural scale l_c. Furthermore, from the available data, a nearly bimodal behavior seems to emerge, with different screening lengths. For instance, $\langle\widetilde{\delta T}\rangle_2$ drops at $x \sim 16l_c$ by factors about 3 and 10 for the two groups of curves in Fig11. However, the parameters and mechanisms which govern the decay are not elucidated. The existence of a transition would suggest that the proximity to a percolation threshold plays a role. This could result from a particularly strong influence of mismatches of the inlet and outlet faces, but also from a change of the relevant microscale. In a near-critical state, it switches from the correlation length l_c to the typical size of the conducting clusters (also called "correlation length" in the framework of percolation theory, but with a different meaning).

5. Undersampling : measurements in inner subdomains

The conductivity tensors associated with central sub-blocks of the samples have been systematically evaluated according to the procedure described in Section 2.8. A tensor $\mathbf{\Lambda}_{[BC],c}(M)$ can be deduced via (8) from the set of $\langle\mathbf{q}\rangle_c$ and $\langle\nabla T\rangle_c$ vectors measured in a series of concentric subdomains $\Omega_c(M)$ obtained by removing from Ω a peripheral layer with thickness M, when solving problem (1) submitted to boundary conditions [BC] at $\partial\Omega$. Results are presented in Fig.12 for two examples of PSM with porosity 0.08 and TGF with porosity 0.12, for λ_s/λ_g=10^{-3}. A similar figure for FS and BS can be found in [1].

The porosity ε is shown on the left as a function of M, for the 4 stochastic realizations and their average. Its statistical fluctuations increase with M as the volume of the measuring domain decreases, but since the samples are large, these fluctuations remain quite moderate over the broad range $M \lesssim 160p_x$ ($\pm$0.002 for PSM and $\pm$0.005 for

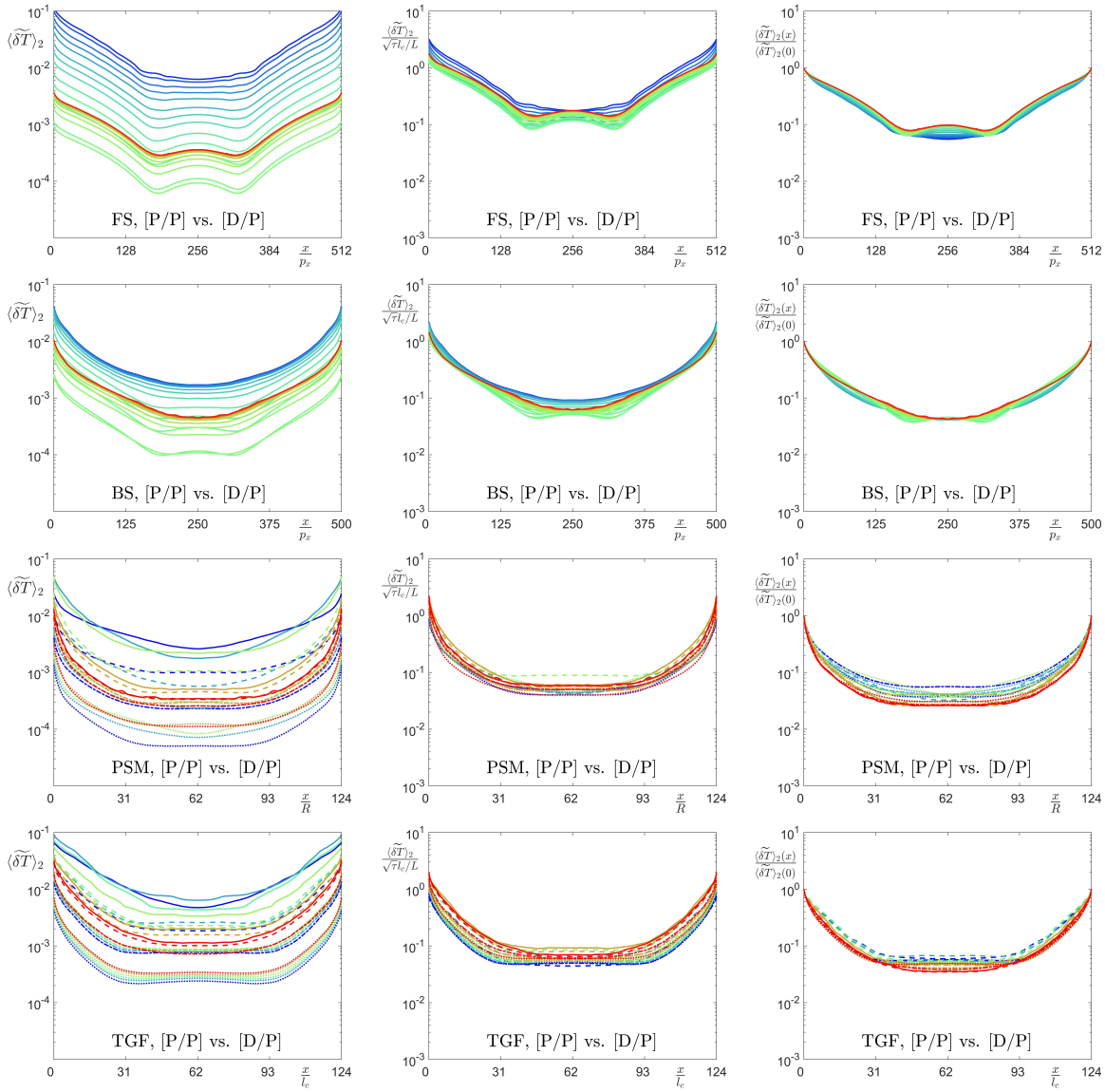

Figure 10: Profiles of $\langle\widetilde{\delta T}\rangle_2$ along the mean gradient direction in FS, BS, PSM and TGF (top to bottom rows), for BC's [D/P] and [P/P]. Raw value (left column), $\langle\widetilde{\delta T}\rangle_2$ normalized by $\sqrt{\tau}l_c/L$ (middle) and by the value of $\langle\widetilde{\delta T}\rangle_2$ at the outer boundary (right). Colors for FS and BS correspond to the contrast λ_s/λ_g, with the convention of fig.4a. Line types and colors for PSM and TGF correspond to the contrast λ_s/λ_g and porosity ε, respectively, with the conventions of fig.4b-d.

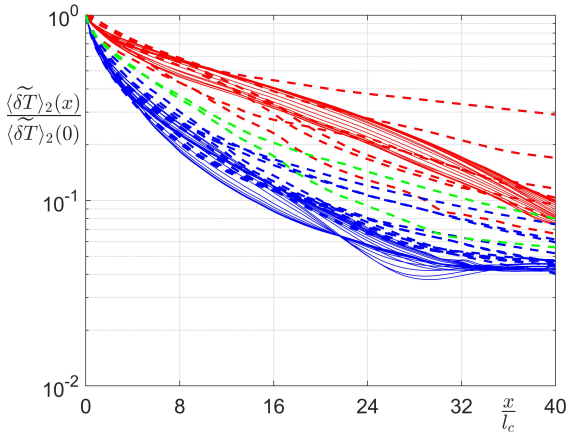

Figure 11: Decay of $\langle\widetilde{\delta T}\rangle_2$ with the distance x from the boundary normalized by the correlation length l_c, for [D/P] vs. [P/P]. The blue curves include all the data for BS (solid lines) and those for the synthetic media with $\lambda_s/\lambda_g \geq 10^{-3}$ and large porosities (ε >0.08 for PSM and 0.15 for TGF, broken lines). The red curves include all the data for FS (solid lines)and those for the synthetic media with λ_s/λ_g=10^{-4} and small porosities ($\varepsilon \leq$0.08 for PSM and 0.15 for TGF, broken lines). Green broken lines correspond to PSM (ε =0.08) and TGF (ε =0.15) with $\lambda_s/\lambda_g = 10^{-3}$.

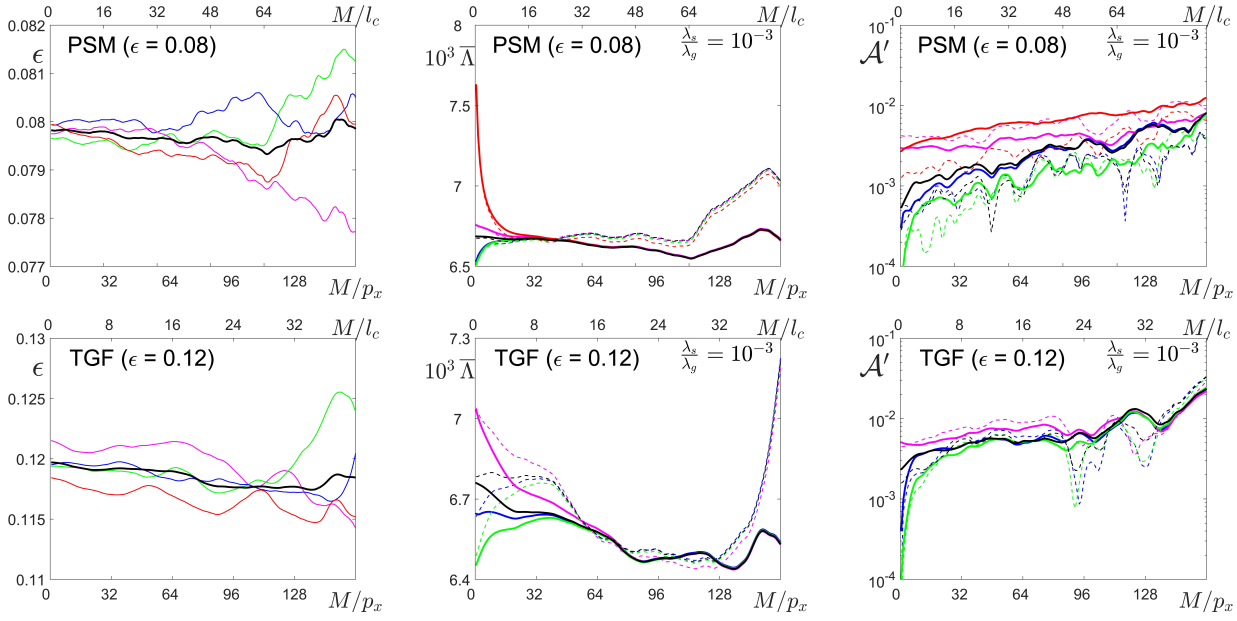

Figure 12: Measurements in inner domains $\Omega_c(M)$, for samples PSM with porosity 0.08 (top) and TGF with porosity 0.12 (bottom). Porosity ε (left column), mean conductivity $\overline{\Lambda}_c$ (middle) and asymmetry index $\mathscr{A}_c'$ (left) are plotted vs. the removed layer thickness M. Colors for $\overline{\Lambda}_c$ and $\mathscr{A}_c'$ correspond to the applied BC's with the convention of Fig.4e. λ_s/λ_g=10^{-3}. The porosity $\varepsilon(M)$ is shown for 4 individual samples (colors) and for their average (black). $\overline{\Lambda}_c$ and $\mathscr{A}_c'$ are shown for a single realization (broken lines, corresponding to the blue $\varepsilon(M)$ curve), and in arithmetic (for $\overline{\Lambda}_c$) or RMS (for $\mathscr{A}_c'$) average over the four samples (solid lines).

TGF). Thus a range with M thick enough to screen most of the influence of the BC's while Ω_c remains large enough to be representative can exist in these examples.

The plots of the mean diagonal terms $\overline{\Lambda}_c$ resulting from various overall BC's confirm this expectation (middle column in Fig.12). The values of $\overline{\Lambda}$ for M=0 differ by as much as 20% in the PSM sample, but $\overline{\Lambda}_c$ for [D/D] which departs the most from the other predictions drops very fast, so that all predictions are within $\pm 5\%$ as soon as $M \geq 4l_c \approx 2R$. This is because the measuring volume Ω_c excludes the conducting skin caused by [D/D] shown in Fig.9. This feature does not show in the example for TGF since [D/D] was not implemented for this model, but it is clearly visible as well in the similar plots of Fig.11 of [1] for FS and BS. For larger M, all predictions $\overline{\Lambda}_c$ converge progressively, and reach a very good agreement when $M \sim 16l_c$ (within about $\pm 1\%$, and all distances $\mathscr{D}' \leq 10^{-2}$, see Fig.13). The differences of the local temperature fields are not entirely screened out at this distance (green curves in Fig.11), but their absolute values are small: $\langle \widetilde{\delta T} \rangle_2 \lesssim 2\ 10^{-3}$ for PSM and $8\ 10^{-3}$ for TGF in Fig.10. All these comments apply both to the data for an individual sample and to the average over samples shown in Fig.12.

It is worth mentioning here the investigation in [31] of the permeability and electrical conductivity (corresponding to λ_s/λ_g=0) of several rock samples, based on tomographic images of cylindrical samples. The influence of the removal of a transverse peripheral layer was examined and the convergence of the predictions from two different kinds of boundary conditions was demonstrated, as for $\overline{\Lambda}_c$ in Fig.12. In these materials, the influence of the transverse BC, which corresponds to the deviations observed near the top and bottom boundaries in Fig.8b, is felt up to a distance of 3–4 pores away from the boundary for the permeability and less than that for the electical conductivity.

Finally, the asymmetry index $\mathscr{A}'_c$ of $\overline{\Lambda}_c$ in the right column of Fig.12 is seen to increase with M. It does not reach alarming levels in the present examples, but larger values are observed in cases of larger constrasts and/or smaller porosities (*e.g.*, $\approx$0.05 for FS in Fig.11 of [1]). Recall that $\overline{\Lambda}_c$ differs by at least $\mathscr{A}'_c$ from any acceptable conductivity tensor, as discussed in Section 2.9. Therefore, this minimal degree of uncertainty should be kept in mind even if concordant predictions of the effective conductivity are obtained from different upscaling procedures.

A more complete set of data covering the whole range of contrasts λ_s/λ_g is presented in Fig.13, where the distances $\mathscr{D}'(\mathbf{\Lambda}_{[BC_1],c}, \mathbf{\Lambda}_{[BC_2],c})$ are plotted as functions of M. This accounts more fully for all the differences between tensors, including in their individual eigenvalues and eigendirections, than the mere comparison of the mean diagonal $\overline{\Lambda}_c$. The figure includes FS and BS, and the individual realizations of PSM and TGF considered in Fig.12. Other realizations and their statistical averages give rise to similar features. Synthetic media with different porosities also present the same patterns, although the positions of the transitions can be shifted. However, we do not intend here to provide a comprehensive survey of the evolution of the distances between conductivity tensors measured in sub-volumes, which we could not fully rationalize anyway. Instead, our purpose is to illustrate the main phenomenological features to be expected in the practical application of the undersampling approach to a particular sample. Recall also that values of $\mathscr{D}' \lesssim 10^{-3}$ are mostly indicative, as pointed out in Section 3.

The general features observed in Fig.6 for the distances between the overall tensors $\mathbf{\Lambda}$ also apply to their values $\mathbf{\Lambda}_c$ in inner sub-domains. $\mathscr{D}'$ increases with the contrast in the component conductivities, and tends toward asymptotic values when the contrast is large. When the solid is the most conducting phase, the pictures obtained for all $\lambda_s/\lambda_g \geq 10$ are very similar, and only those for $\lambda_s/\lambda_g = 100$ are shown for FS and BS. The hierarchy of the distances is also preserved. Distances $\mathscr{D}'$ for pairs of BC's involving [D/D] (reddish curves) are always larger than the others for $\mathbf{\Lambda}$, and remain so even when the measurement $\mathbf{\Lambda}_c$ is restricted to inner sub-domains. There is no clear-cut general behavior, but the following observations can be made.

- $\mathscr{D}'$ decreases steeply as the thickness M of the layer discarded for the measurements increases from zero.

- $\mathscr{D}'$ slowly increases with M, when it becomes very large. The reason for this is unclear, but it is of no concern since $\mathscr{D}'$ is always small in this range ($\lesssim 10^{-2}$).

- Consequently, there is a minimum for $\mathscr{D}'$ at some intermediate position. The transition between the decaying and growing regimes can be smooth, sometimes with the appearence of a plateau, or more acute. The minimum takes place around $M \sim 16l_c$ in BS, PSM and TGF when the contrast is strong, and sooner than that if the contrast is mild. It occurs later in FS, in keeping with the differences in screening lengths observed in Fig.11. FS belongs to the set of slowly decaying red curves, while BS and the samples of synthetic media with λ_s/λ_g=10^{-3} belong to the sets of steeper blue and green curves, respectively.

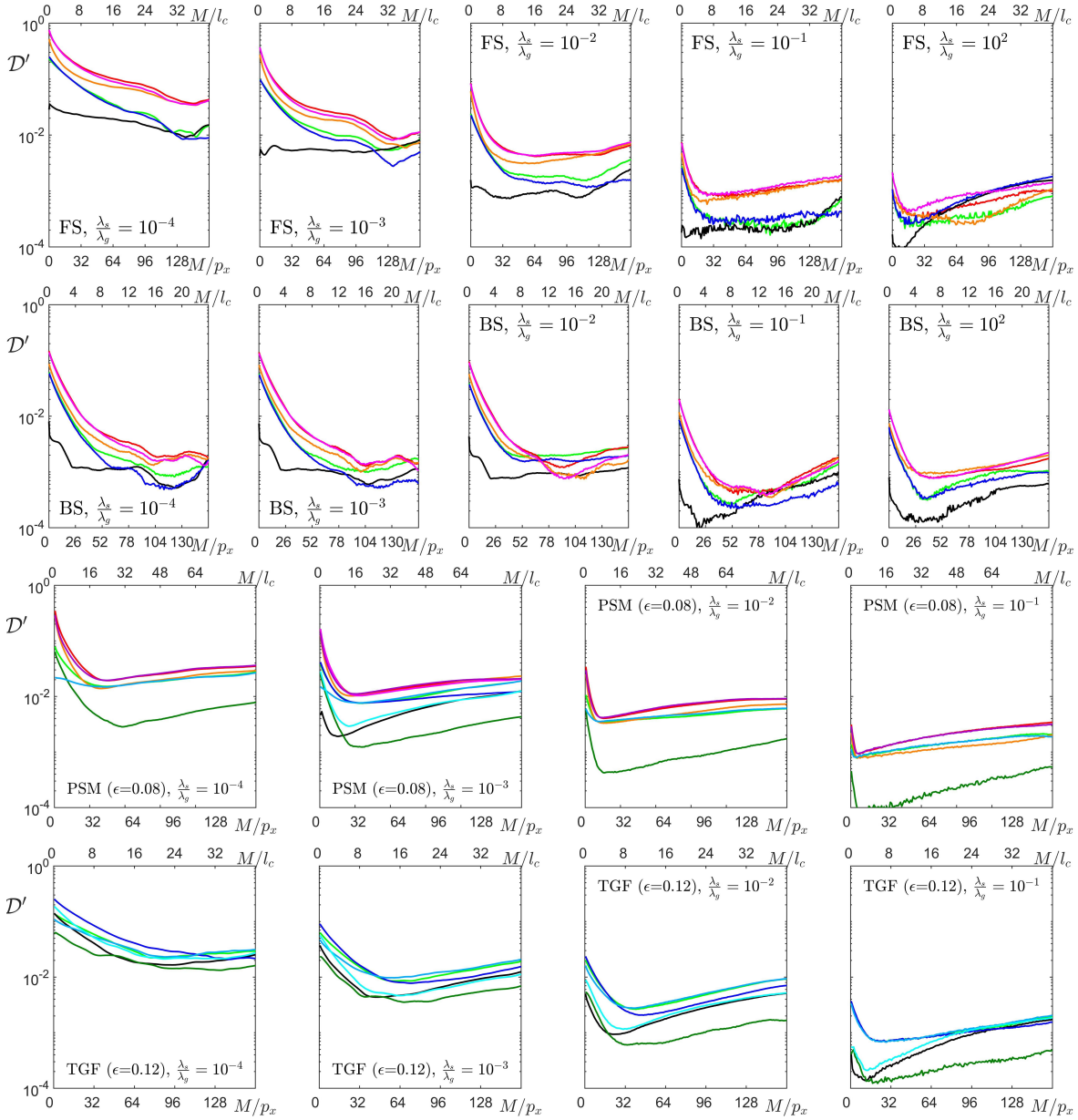

Figure 13: The distances $\mathscr{D}'(\mathbf{\Lambda}_{1,c}, \mathbf{\Lambda}_{2,c})$ between the tensors obtained in inner domains $\Omega_c(M)$ with various BC's, as functions of the removed layer thickness M. Data are for samples FS, BS, PSM (ε=0.08) and TGF (ε=0.08), from top to bottom, with $\lambda_s/\lambda_g = 10^{-4}$ to 10^{-1}, from the left to the right. Additional plots are shown for FS and BS with $\lambda_s/\lambda_g = 10^2$ (rightmost). Colors correspond to the pairs of BC's applied at the outer boundaries with the convention in Fig.4f.

In the examples in Fig.13, the cases which call for attention because the various determinations of $\mathbf{\Lambda}$ depart by distances $\mathscr{D}'$ of order O(10^{-1}) or more correspond to $\lambda_s/\lambda_g \leq 10^{-2}$ for FS and BS and $\leq 10^{-3}$ for PSM and TGF. Undersampling is a possible way to try and filter out the influence of the BC's, and indeed, its application with $M = 16 l_c$ in all these cases yields tensors $\mathbf{\Lambda}_c$ which are all in agreement within a reasonable practicle tolerance of $\mathscr{D}' \leq 0.05$, and often much less. The only exception is FS with $\lambda_s/\lambda_g \leq 10^{-4}$, but the remaining deviations of the order of O(10^{-1}) involve the [D/D] conditions and it disappears if this inadvisable BC is discarded.

Note that Fig.13 is incomplete in the sense that it only compares tensors $\mathbf{\Lambda}_{[BC],c}$ from various BC's in the same subdomains, not their values in domains of different sizes. In order to be an intrinsic, effective parameter, the tensor should also be invariant over a range of M. This is partly checked in Fig.12 with the plots of $\overline{\Lambda}_c$, which is indeed found constant within $\pm 1.5\%$ in a range $16 \leq M/l_c \leq 64$ for PSM and $16 \leq M/l_c \leq 32$ for TGF. This is a promising but partial indication. To be rigorous, both checks for the independence on the BC's and on the domain size have to be made by use of the tensorial distance $\mathscr{D}'$. For the sake of concision, only the former is presented in these terms here.

All the quantitative statement in the above applies of course only to the particular examples considered in this section, and should not be blindly transposed to other materials, such as PSM or TGF with different porosities or media of an entirely different kind. The observed general features are expected to apply qualitatively in any case, but not quantitatively when applying the undersampling in any particular sample.

6. Discussion and conclusions

The impact of the choice of boundary conditions on the macroscopic transport coefficient predicted by a numerical upscaling has been systematically investigated for a variety of real or model heterogeneous materials, with broad ranges of geometrical properties and conductivity contrasts, by considering five kinds of BC's. The differences of the various predictions have been quantified by the tensorial distance $\mathscr{D}'$.

Note first that when the conductivity contrast is very large, its precise value makes ultimately no difference and the macroscopic coefficients are in practice equivalent to those for infinite contrast. For instance, if the solid tends to be insulating (likewise in the opposite limit), the tensors $\mathbf{\Lambda}_{[BC]}$ and therefore their differences $\mathscr{D}'$ converge as

$$\mathbf{\Lambda}_{[BC]} \to \lambda_g \, \mathbf{\Lambda}^{(1,0)}_{[BC]} \qquad \text{and} \qquad \mathscr{D}'\left(\mathbf{\Lambda}_{[BC1]}, \mathbf{\Lambda}_{[BC2]}\right) \to \mathscr{D}'\left(\mathbf{\Lambda}^{(1,0)}_{[BC1]}, \mathbf{\Lambda}^{(1,0)}_{[BC2]}\right) \qquad \text{as } \lambda_s/\lambda_g \to 0 \tag{14}$$

where $\mathbf{\Lambda}^{(1,0)}_{[BC]}$ is the tensor obtained when λ_g=1 and λ_s=0. These convergences are indeed observed, but their asymptotic values are not reached yet in some cases in the investigated range of contrast. This occurs in situations of strong contrasts with a sparse and/or poorly connected conducting phase, *i.e.*, $\Lambda \ll \langle \lambda \rangle$ or $\tau \gg 1$, which are also those where one should be the most concerned about the influence of the boundary conditions, and where the numerical calculations are computionally most demanding. However, the fact that the ratio $\mathscr{D}'/\tau$ is nearly independent of the contrast (middle row in Fig.6) is a new piece of information and advantage can be taken from it to infer the expected uncertainty for a strong contrast from its knowledge for a milder one.

The additional feature that the BC's effects scale as the inverse of the sample size and the corresponding normalization of $\mathscr{D}'$ by l_c/L contributes to unify even more the data and leads to the representation of the whole set of numerical results in Fig.7. For any particular sample, the values of $\mathscr{D}'$ for various pairs of BC's measure the difference of the corresponding predictions of $\mathbf{\Lambda}$. Some pairs such as ([P/P],[E+P]) are always in a better agreement than others, but the largest $\mathscr{D}'$ can be considered as an estimate of the intrinsic uncertainty of the determination of $\mathbf{\Lambda}$, since at least two results differ by that much. Thus, only the upper envelope of the data is to be considered. It is fairly well described by (13), where the uncertainty is simply proportionnal to $\tau l_c/L$.

The observation (13) is probably the most important result in this paper. It provides a practical *a priori* criterion to estimate an upper bound of the relative uncertainty of a tensor obtained by numerical upscaling. When the data required for the solution of problem (1) are available, l_c and $\langle \lambda \rangle$ are readily available as well. When a calculation with some BC yields a tensor $\mathbf{\Lambda}$, τ can be estimated and (13) tells by how much tensors resulting from other BC's could differ from $\mathbf{\Lambda}$. Recall that $\mathscr{D}'$ is the value that the relative error of the flux can reach when $\mathbf{\Lambda}$ is used in simulations (see section 2.9).

There are actually two envelopes in Fig.7 and two estimates of the uncertainty in (13), according to whether the immersion conditions [D/D] should be considered or not. This question is raised by the *a priori* suspicion that [D/D] introduces by itself spurious effects discussed in Section 2.6, and by the observation that indeed, it often yields predictions notably different (larger) from those from other BC's. The reservations about [D/D] are supported by the analysis of local fields.

Their comparison for different BC's in Section 4 reveals various phenomenological features. Is is observed that the RMS deviations of the local fields scale as $\sqrt{\tau}$, and that their magnitude decays within the samples over a screening distance which is not simply proportional to the textural length l_c. A nearly bimodal behavior seems to emerge, with different screening lengths according to whether or not the material is close to a critical state regarding conduction. The latter feature is not understood, and might deserve further investigation. However, it is made unambiguously apparent that [D/D] causes the appearance of an excess flux in a peripheral skin along the transverse boundaries, which explains the larger predicted macroscopic conductivity.

Hence, we advocate that using the [D/D] immersion condition is inadvisable, because it introduces by itself strong artefacts. It induces thereby large values of the distance $\mathscr{D}'$ from the predictions with other BC's, but mostly due to its own identified sources of error. Recall also that the permeameter conditions or the periodization of the sample by justaposition of mirrored replicas have not been considered here because they are known to constrain the eigendirections of $\mathbf{\Lambda}$. Rotating them would induces large values of $\mathscr{D}'$ if the medium is not very close to isotropic. If such approaches as well as [D/D] are set aside, (13b) applies.

In summary, (13) provides a criterion for the *a priori* detections of situations that might be problematic in practical applications. Once a numerical upscaling has been performed, $\tau l_c/L$ is readily available and if it is too large, it is very likely that a solution of (1) with another BC would yield a significantly different result. Recall that a noticeable asymmetry is also a worrying feature, since the index $\mathscr{A}'$ is a lower bound for the distance of $\mathbf{\Lambda}$ from any acceptable value (see Section 2.9). In case of doubts, appropriate measures should then be taken. The first step could be to try different BC's, and check whether the result is really impacted. If it is, the next step might be to consider ways to filter out the BC's influence, by excluding the potentially disturbed region from the measurement volume.

To this end, we recommend the undersampling procedure described in Section 2.8 and illustrated in Section 5 for various examples. It should be emphasized that it is virtually cost-free. Once problem (1) has been solved with any kind of BC, measuring the mean flux $\langle \mathbf{q} \rangle_c$ and gradient $\langle \nabla T \rangle_c$ in a series of inner sub-domains does not require any significant additional computational effort. The conductivity tensors $\mathbf{\Lambda}_{[BC],c}$ resulting from various BC's should be compared. Hopefully, $\mathbf{\Lambda}_{[BC],c}$ can be found identical for all BC's and in a wide enough range of sub-domains sizes (within a user-defined tolerance for $\mathscr{D}'$). This tensor can be then regarded as an intrinsic effective property, associated with and only with the material under consideration. This requires that the sample is large enough so that a peripheral layer can be discarded from the measurement volume, sufficiently thick to screen out most of the BC's influence, while the remaining volume is still large enough to be representative. If this is not possible, it must be accepted that no reliable estimate of an effective conductivity tensor can be obtained from this sample.

Acknowledgements

This work pertains to the French Government Programme "Investissements d'Avenir" (LABEX INTERACTIFS, reference ANR-11-LABX-0017-01).

References

[1] J. Shi, G. Boyer, V. Mourzenko, J.-F. Thovert, On the influence of boundary conditions when determining transport coefficients from finite samples of porous media. assessment for tomographic images of real materials, Transp Porous Med 132 (2020) 561–590. doi:https://doi.org/10.1007/s11242-020-01404-1.

[2] S. Hubbard, Y. Rubin, Hydrogeological parameter estimation using geophysical data: a review of selected techniques, Journal of Contaminant Hydrology 45 (2000) 3–34. doi:https://doi.org/10.1016/S0169-7722(00)00117-0.

[3] J. C. S. Long, J. S. Remer, C. R. Wilson, P. A. Witherspoon, Porous media equivalents for networks of discontinuous fractures, Water Resours. Res. 18 (3) (1982) 645–658. doi:https://doi.org/10.1029/WR018i003p00645.

[4] P. Spanne, J.-F. Thovert, C. J. Jacquin, W. B. Lindquist, K. W. Jones, P. M. Adler, Synchrotron computed microtomography of porous media. Topology and transports, Phys. Rev. Lett. 73 (1994) 2001–2004. doi:https://doi.org/10.1103/PhysRevLett.73.2001.

[5] P. Renard, G. de Marsily, Calculating equivalent permeability: a review, Advances in Water Resources 20 (5–6) (1997) 253–278. doi:https://doi.org/10.1016/S0309-1708(96)00050-4.

[6] L. J. Durlofsky, Upscaling and gridding of fine scale geological models for flow simulation, in: 8th International Forum on Reservoir Simulation, Iles Borromees, Stresa, Italy, 2005.

[7] H. Andrä, N. Combaret, J. Dvorkin, E. Glatt, J. Han, M. Kabel, Y. Keehm, F. Krzikalla, M. Lee, C. Madonna, M. Marsh, T. Mukerji, E. Saenger, R. Sain, N. Saxena, S. Ricker, A. Wiegmann, X. Zhan, Digital rock physics benchmarks – part II: computing effective properties, Computers & Geosciences 50 (2013) 33–43. doi:https://doi.org/10.1016/j.cageo.2012.09.008.

[8] P. S. Lang, A. Paluszny, R. W. Zimmerman, Permeability tensor of three-dimensional fractured porous rock and a comparison to trace map predictions, JGR: Solid Earth 119 (2014) 6288–6307. doi:https://doi.org/10.1002/2014JB011027.

[9] X. Wu, Y. Efendiev, T. Hou, Analysis of upscaling absolute permeability, Discrete Contin. Dyn. Syst. Ser. B 2 (2002) 185–204. doi:https://doi.org/10.3934/dcdsb.2002.2.185.

[10] J. J. Gomez-Hermindez, A. G. Journel, Stochastic characterization of grid-block permeabilities: from point values to block tensors, in: D. Guerillot, O. Guillon (Eds.), 2nd European Conference on the Mathematics of Oil Recovery, Edition Technip, Paris, 1990, pp. 83–90. doi:https://doi.org/10.3997/2214-4609.201411102.

[11] X. H. Wen, L. J. Durlofsky, M. G. Edwards, Use of border regions for improved permeability upscaling, Mathematical Geology 35 (2003) 521–547. doi:https://doi.org/10.1023/A:1026230617943.

[12] M. Piller, G. Schena, M. Nolich, S. Favretto, F. Radaelli, E. Rossi, Analysis of hydraulic permeability in porous media: From high resolution X-ray tomography to direct numerical simulation, Transp Porous Med 80 (2009) 57–78. doi:https://doi.org/10.1007/s11242-009-9338-9.

[13] R. Guibert, P. Horgue, G. Debenest, M. Quintard, A comparison of various methods for the numerical evaluation of porous media permeability tensors from pore-scale geometry, Math Geosci 48 (2016) 329–347. doi:https://doi.org/10.1007/s11004-015-9587-9.

[14] K. Gerke, M. Karsanina, R. Katsman, Calculation of tensorial flow properties on pore level: Exploring the influence of boundary conditions on the permeability of three-dimensional stochastic reconstructions, Phys. Rev E 100 (2019) 053312. doi:https://doi.org/10.1103/PhysRevE.100.053312.

[15] J.-F. Thovert, F. Yousefian, P. Spanne, C. G. Jacquin, P. M. Adler, Grain reconstruction of porous media: application to a low-porosity Fontainebleau sandstone, Phys. Rev. E 63 (6) (2001) 61307–61323. doi:https://doi.org/10.1103/PhysRevE.63.061307.

[16] J.-F. Thovert, P. M. Adler, Grain reconstruction of porous media: Application to a Bentheim sandstone, Phys. Rev E 83 (056116). doi:https://doi.org/10.1103/PhysRevE.83.056116.

[17] P. M. Adler, C. G. Jacquin, J. A. Quiblier, Flow in simulated porous media, Int. J. Multiphase Flow 16 (4) (1990) 691–712. doi:https://doi.org/10.1016/0301-9322(90)90025-E.

[18] P. M. Adler, Porous Media: Geometry and Transports, Butterworth/Heinemann, Stoneham, MA, 1992.

[19] M. Quintard, S. Whitaker, Transport in ordered and disordered porous media: volume-averaged equations, closure problems, and comparison with experiment, Chemical Engineering Science 48 (14) (1993) 2537–2564. doi:https://doi.org/10.1016/0009-2509(93)80266-S.

[20] A. Bourgeat, M. Quintard, S. Whitaker, Eléments de comparaison entre la méthode d'homogénéisation et la méthode de prise de moyenne avec fermeture, C. R. Acad. Sciences Paris 306 (serie II) (1988) 463–466.

[21] A. Henriette, C. G. Jacquin, P. M. Adler, The effective permeability of heterogeneous porous media, PhysicoChemical Hydrodynamics 11 (1) (1989) 63–80.

[22] D. A. G. Bruggeman, Berechnung verschiedener physikalischer konstanten von heterogenen substanzen, Annalen der Physik 24 (1935) 636–679. doi:https://doi.org/10.1002/andp.19354160705.

[23] R. Landauer, Electrical conductivity in inhomogeneous media, in: AIP Conference Proceedings, Vol. 40, 1978, pp. 2–43. doi:https://doi.org/10.1063/1.31150.

[24] M. Knackstedt, C. Arns, M. Saadatfar, T. Senden, A. Limaye, A. Sakellariou, A. Sheppard, R. Sok, W. Schrof, H. Steininger, Elastic and transport properties of cellular solids derived from three-dimensional tomographic images, Proc. R. Soc. A. 462 (2006) 2833–2862. doi:http://doi.org/10.1098/rspa.2006.1657.

[25] A. Pouya, O. Fouché, Permeability of 3D discontinuity networks: new tensors from boundary-conditioned homogenisation, Advances in Water Resources 32 (3) (2009) 303–314. doi:https://doi.org/10.1016/j.advwatres.2008.08.004.

[26] J.-L. Auriault, Heterogeneous periodic and random media. are the equivalent macroscopic descriptions similar?, Int. J. Engineering Science 49 (2011) 806–808. doi:https://doi.org/10.1016/j.ijengsci.2011.01.005.

[27] Z. Hashin, S. Shtrikman, A variational approach to the theory of the elastic behaviour of multiphase materials, Journal of the Mechanics and Physics of Solids 11 (2) (1963) 127–140. doi:https://doi.org/10.1016/0022-5096(63)90060-7.

[28] A. Ralston, P. A. Rabinowitz, First Course in Numerical Analysis, Dover Publications, Mineola, N.Y., 2001.

[29] R. Guibert, M. Nazarova, P. Horgue, G. Hamond, P. Creux, G. Debenest, Computational permeability determination from pore-scale imaging: sample size, mesh and method sensitivities, Transp Porous Med 107 (2015) 641–656. doi:https://doi.org/10.1007/s11242-015-0458-0.

[30] K. Guan, M. Nazarova, B. Guo, H. Tchelepi, A. Kovscek, P. Creux, Effects of image resolution on sandstone porosity and permeability as obtained from x-ray microscopy, Transp Porous Med 127 (2019) 233–245. doi:https://doi.org/10.1007/s11242-018-1189-9.

[31] S. Alizadeh, S. Latham, J. Middleton, A. Limaye, T. Senden, C. Arns, Regional analysis techniques for integrating experimental and numerical measurements of transport properties of reservoir rocks, Adv. Wat. Res. 100 (2017) 48–61. doi:http://dx.doi.org/10.1016/j.advwatres.2016.12.011.